Relationship between Growth Faults and Subsidence:
Impact on Coastal Erosion, an Example from Cameron Parish, Southwestern Louisiana, USA

A Thesis

Presented to

The Graduate Faculty of the

University of Louisiana at Lafayette

In Partial Fulfillment of the

Requirements for the Degree

Master of Science

Matthew Covington O'Leary

Summer 2018

Relationship between Growth Faults and Subsidence:

Impact on Coastal Erosion, an Example from Cameron Parish, Southwestern Louisiana, USA

Matthew Covington O'Leary

APPROVED:

Raphael Gottardi, Chair
Assistant Professor of Geology

Gary Kinsland
Professor of Geology

Tim Duex
Professor of Geology

William Finley
Adjunct Instructor of Geology

Mary Farmer-Kaiser
Dean of the Graduate School

O'Leary, Matthew Covington Bachelor of Science, Louisiana State University, Spring 2015; Master of Science, University of Louisiana at Lafayette, Summer 2018
Major: Geology
Title of Thesis: Relationship between Growth Faults and Subsidence: Impact on Coastal Erosion, an Example from Cameron Parish, Southwestern Louisiana
Thesis Director: Dr. Raphael Gottardi
Pages in Thesis: 102 Words in Abstract: 227

Abstract

This study investigates the relationship between faulting, subsidence, and land loss in coastal Louisiana. A methodology that integrates 3D seismic data, well logs, high-resolution topographic mapping (LIDAR), and historical aerial photography is successfully developed to identify fault-related geomorphic changes in southwestern Louisiana's Chenier Plain. Analysis of a 3D seismic survey and well logs reveals the presence of 10 normal faults that form an east-west graben in the middle of the study area. Well logs were used to further constrain the geometry of the faults. Shallow water well logs were used to map the faults at shallow depth, below the resolution of the seismic survey. Fault traces were extrapolated to the surface by maintaining constant dip, and projected on LIDAR data. Elevation profiles derived from the LIDAR were conducted across the different faults, and results show that there is a distinct difference between the upthrown and downthrown sides of the faults. Historical aerial photographs were used to investigate any change in geomorphology from 1953 to 2017 within the study area. Results reveal the occurrence of water bodies on the immediate downthrown sides of suspected fault traces. Our findings suggest that faulting influences and focuses areas where subsidence is happening and subsequent land loss may occur and detailed understanding of active shallow faulting in coastal area can be used to identify regions that are at risk of land loss.

Acknowledgments

I would like to thank Seismic Exchange, Inc. (SEI), Miami Corporation, and DOR Lease Services Inc. for providing the necessary data and work space for this research. Without these assets, this thesis would not have been possible. I would like to thank Mr. Chris McLindon for introducing me to this type of project. I would also like to thank Mr. William Finley for his unrivaled mentorship, reminding me the answer is always no if you never ask the question and to use all the available data. In addition, I would like to thank Dr. Raphael Gottardi for his excellent guidance and assistance in finishing this endeavor. Furthermore, I would like to thank my additional thesis committee members, Dr. Gary Kinsland and Dr. Tim Duex, for their attention to detail, teachings of geology, and stories. A big thank you to my family for their love and support throughout this entire process, especially my father, Bill O'Leary, for inspiring me to become a geologist. Lastly, to my friends, grad school and Clark Ct. would not have been the raucous good time it was without y'all.

Table of Contents

List of Figures

List of Tables

1.   Introduction

1.1.   Purpose

This study is part of a broader research initiative that was started two years ago by the New Orleans Geologic Society (NOGS), which aims at investigating whether shallow faulting has an impact on coastal areas. Gagliano (2003) identified surface geomorphic signatures of faults that are surface traces and scarps of suspected faults from maps, aerial images, published descriptions and personal interviews. These surface features correlated with north-south megaregional sections and known regional faults from the regional framework map (Geomap South Louisiana Executive Reference Maps). Gagliano (2003) hypothesized that most of the massive land loss in coastal Louisiana during the twentieth century resulted from fault induced subsidence. Gagliano's (2003) analysis focused in southeastern Louisiana, on the Mississippi river delta. This thesis aims at studying the same problems, i.e. investigating the relationship between faulting, subsidence, and land loss but focusing on a different geologic setting: the Chenier Plains of southwestern Louisiana. The hypothesis is that land loss has an identifiable geomorphology as a consequence of shallow faulting, growth fault activity, and surface distortions or subsidence. To test our hypothesis, we use a combination of surface and subsurface datasets. A 3D Seismic survey provided by Seismic Exchange Inc. is analyzed to delineate shallow faults. Fault traces are then projected to the surface and correlated to surface geomorphology, to investigate their role on coastal subsidence. Light Detection and Ranging (LIDAR) data and aerial imagery are used to confirm the expression of these faults at the surface. The history of fault movement and rates of subsidence is determined through stratigraphy, thickness differentials, and growth index, by using subsurface well log correlation.

The results of this study constrain the role of fault and subsidence on land loss along the Louisiana coastline in Cameron Parish. LIDAR elevation data across profiles straddling the fault traces shows vertical difference between the up- and downthrown side ranging from ~1.5 inches to as much as 6.6 inches. Historical aerial photograph ranging from 1953 to 2017 were used to investigate changes in surface geomorphology, revealing the occurrence of water bodies on the immediate downthrown sides of suspected fault traces. The results of this study suggest that faulting plays a strong role in controlling subsidence, and possible land loss. The methodology used in this study should be applied along the Louisiana coastline to identify areas of active shallow faulting as they might be at greatest risk of further land loss.

1.2. Overview

The study area is located in southwestern Louisiana, specifically within Cameron Parish, west of Grand Lake, and is part of Louisiana's Gulf Coast (Figure 1). This region has been characterized as part of the Chenier Plains. The Chenier Plains can be classified as a low profile, storm-dominated, micro-tidal coast, down drift, and west of the Mississippi River deltaic plain (Owen, 2008). The plain consists of interspersed Holocene sediments resting unconformably on Pleistocene aged Prairie Terrace deposits (Gould and McFarlan, 1959). Holocene deposits are primarily mudflats capped by marsh with interspersed thin sand and shell rich ridges called cheniers, meaning "*place of many oaks*" (Russell and Howe, 1935). These sediments overlay the Prairie Terrace which is characterized by Pleistocene aged fluviatile deposits. The formation of Chenier Plains relates back to the delta-lobe switching of the Mississippi River before it was constrained by anthropogenic structures to its present day channel. When the Mississippi River shifted west, the fine-grain sand- and shell-rich sediment would deposit. When it was further away to the east, coastal wave energy and tides

2

would winnow the fines out of deposit leaving behind a sandy beach with an abundance of sand and shell rich ridges (relict open-gulf shorelines). The oldest of these cheniers are found landward and date back to 3000 years old. Currently, the Chenier Plains of southwest Louisiana's Cameron Parish are experiencing a high degree of subsidence, 0.35 in/year (Nienhuis et al, 2017), which is a contributing cause to land loss along the Louisiana coast.

Subsidence results from the compaction and consolidation of young sediments and other activities, both natural and anthropogenic. While low-energy waves and a micro tidal coastline influence this area's land loss, the cause of subsidence here needs further investigation and this thesis evaluates a connection to activity due to faulting.

Growth faulting is typical of the Gulf Coast and recent studies have documented a connection to subsidence near the present day Mississippi River Delta (Armstrong et al., 2014). Expression of these active faults at the surface have been referred to in the past as "fault-line scarps" (Heinrich, 2000; Gagliano et al., 2003). This term implies steeply dipping, fault-related topographic features, but a majority of the faults in the Gulf Coast region exhibit relatively gentle slopes at the ground surface. Generally, Gulf Coast region sediments are poorly consolidated, resulting in fault deformation in the form of cataclastic flow (Scholz, 1998). Subsequently, faulting near the surface results in a horsetail, rather than a clear fault surface boundary (Heltz, 2005). Heltz (2005) proposed the usage of "fault-related steps" to match better the expression of these faults at the surface.
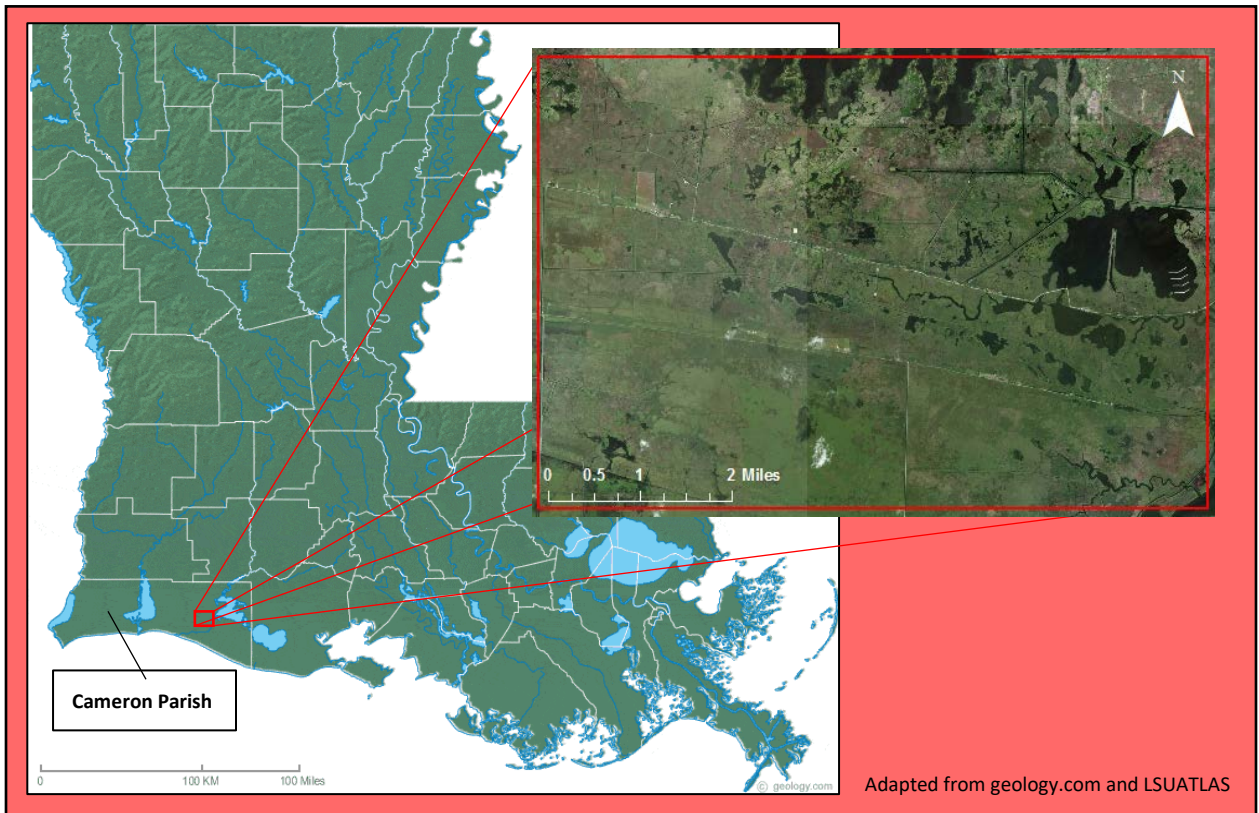
Figure 1: The study area is located in Cameron Parish, southwestern Louisiana.

2.   Methods

This project combines surface and subsurface data. Chris McLindon, of the New Orleans Geological Society, initially proposed the idea of this project. The subsurface part of this study incorporates seismic data provided by Seismic Exchange Inc. (SEI) on Miami Corporation's property as well as well logs from Strategic Online Natural Resources Information System (SONRIS) and the Department of Natural Resources (DNR). Surface data comprised LIDAR and Aerial photographs obtained from the website LSUATLAS and Louisiana State University's Department of Geography and Anthropology's Cartographic Information Center.

2.1.   Analysis of Seismic Data

The seismic data is housed and interpreted at the D-O-R Lease Service Inc. The data itself encompasses an area of 35 square miles. The survey's record length is 8 s with 2001 samples per trace and a sample interval of 0.004 s. The interpretation is limited from 0.3 s to 2.7s time – which was converted to depth using a velocity survey (Table 1). The distance between each seismic trace is 82.5 ft. The seismic survey is interpreted using IHS Markit's, Kingdom. Faults are picked on inlines from west to east, with 20 traces per skip. This way of picking faults is done to set up a simple framework and establish the large faults pertinent to the local and to avoid misinterpreting one fault as another. To ensure all faults are picked, the area is parsed through using two traces per skip. A crossline is used to check the interpretation of the faults. The crossline ensures the accuracy of the interpretation and removes erroneous picks. Fault picks are based on visible offsets between "boomers" – strong seismic reflectors. These fault interpretations are picked to the limit of the seismic data depth Faults that potentially reach the surface, but are lost in the shallow seismic noise, are stopped when offset was not

discernible. A new fault surface is created for these and used to extrapolate where the fault would continue to the surface. These fault picks carry the dip of the deeper surface to ensure consistency across all picks. Based on our interpretation, there are a total of 10 suspected fault surfaces in the study area. Horizons are picked on strong reflector troughs using 2D-Hunt and manual picks.

2.2. Well Log Analysis

Electric logs, primarily resistivity and spontaneous potential (SP) logs, are correlated across several of the faults, using standard techniques of subsurface geologic mapping (see Tearpock and Bischke 1991). Well logs and historical files are obtained through the website SONRIS. A total of 202 oil and gas wells and 45 groundwater wells are imported into the project. These wells were completed between 1937 and 2014. Of the 202 oil and gas wells, 10 electric logs are used for correlation purposes. These 10 logs were found based on their notation of the United States Drinking Water Value indicating that they had logged the shallow section. Most of these are also wildcat wells which typically log shallow depths. These well logs are correlated to depths no deeper than the 6700 ft, the age of which, based on paleo data provided by Paleo – Data, Inc., is approximately Middle Miocene. Main correlations are made between 0 and 2000 ft. Driller logs are obtained from the Department of Natural Resources, ranging from 0 to 800 ft, with a predominance of logs no deeper than 300 ft. These logs contain lithology description with depth. The notes from the driller logs were converted to a color/lithology pattern corresponding to the description in Excel (Figure 2 & 3). These were printed and scanned using a log scanner. This allowed them to be depth registered and brought into kingdom for correlation. Formation tops are assigned based on the log descriptions. Fault surfaces are exported as Landmark X-Y-Z 3D .dat files and

6

brought into a secondary Kingdom Project. A time slice taken at .01 s is used to estimate the

location of fault traces at the surface. These surface traces are then brought into

Lithology	Descriptions
	Shale
	Marsh Mud And clay
	blue clay
	Yellow Clay
	Brown Clay
	Clay
	Clay sand streaks
	Brown tan clay
	Small sand & shale streaks
	big sand gravel
	Coarse Sand
	Grey sand Gravel
	Big sand with gravel
	Big Sand
	Fine Grey Sand
	Medium to coarse sand
	sand
	coarse sand, small p. gravel
	Fine sand
	Top Soil
	Clam Shell
	Clay and Shell
	Medium to coarse sand with gravel
	brown clay and sand streaks
	medium to coarse grey sand with gravel
	Shell
	coarse sand and gravel
	slush
	gumbo
	blue grey clay sand streaks
	fine to medium sand
	silty sand and shell

Figure 2: Log of lithology types and their descriptions for converting driller log notes.

Lith	Depth	Descriptions
6111z		
	0	0-180 clay
	100	
	200	180-220 coarse sand
	300	
	400	
	500	

Figure 3: Example of a typical log made from drillers notes

2.3. ArcGIS's ArcMap

Multiple data types are used for the surface investigation in ArcMap. Aerial images, LIDAR, and other georeferenced data are used for the interpretation. Surface faults traces are overlaid on surface data such as the LIDAR and aerial photographs. Digital elevation models are prepared using ArcMaps 3D analyst and spatial analyst tools. Elevation profiles over areas of interest are done from north to south perpendicular to the strike of the fault. Elevation Profiles are prepared from these. Data points are exported into an excel spreadsheet as a graph of the elevation profile. A 98% exponential smoothing factor is added to illustrate the trend and limit the influence of extreme changes in elevation – abnormal highs or lows (represented by roads or canals). Other information related to the faults surface characteristics is contained in (Appendix, Figure, and Table). From the LIDAR's DEM (Digital Elevation Model) data, the mean area of the upthrown and downthrown sides of suspected fault surface is calculated from Zonal Statistics.

2.3.1. Analysis of LIDAR data.
Light Detection and Ranging, also known as LIDAR, is fundamentally a distance technology. From an airplane or helicopter, LIDAR systems actively send light energy to the ground (Figure 4). This pulse hits the ground and returns to the sensor containing positional information reflected back by distant objects. The raw points are elevation measurements taken with airborne LIDAR, measured in feet. Edited points attempt to represent the bare-earth surface. A digital elevation model (DEM) is an image where the pixels in the image have a value representing elevation in feet taken as an average of the measured points in a 5×5 m area, thus a 5 m resolution. The DEM is derived from the edited points (Figure 5). The vertical accuracy of the points is 6 to 12 in. Subtle

changes in the topography perhaps indistinguishable with the naked eye can be discerned

using LIDAR. This can help identify previously unmapped fault-related steps (Heltz, 2005).
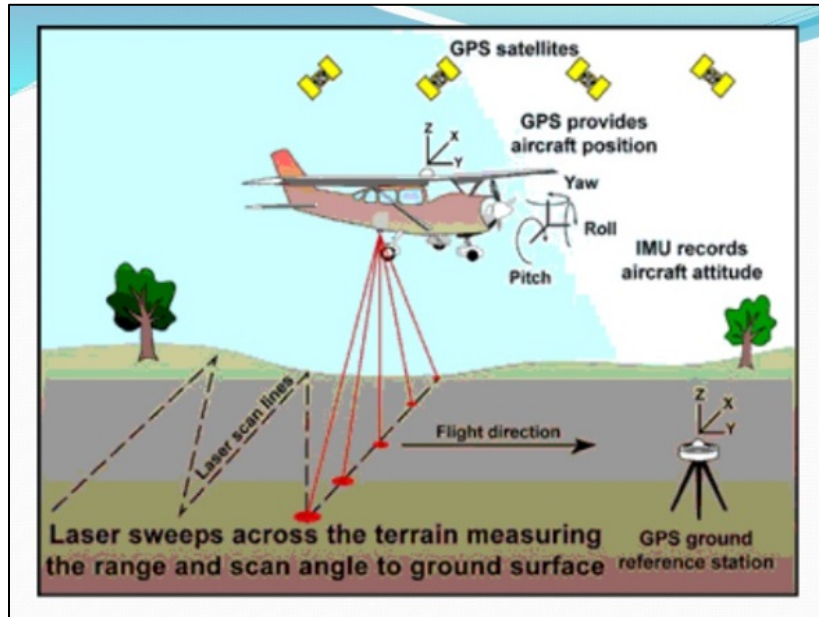
Figure 4: Illustration of LIDAR Capture adapted from Tejistha Pradhan - Student at Sikkim Manipal Institute of Technology
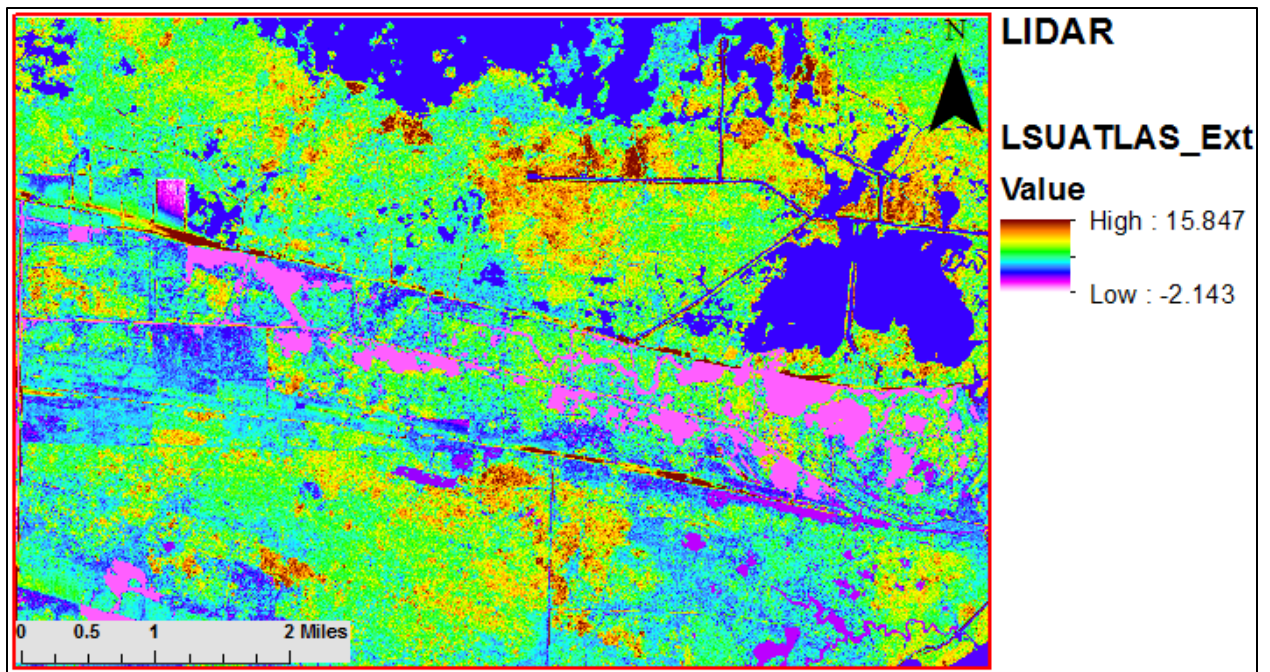
Figure 5: LIDAR DEM image adapted from LSUATLAS

2.4.   Aerial Images

Raster data were obtained by collecting and scanning aerial photographs and satellite images. The aerial images that are housed at Louisiana State University's Department of Geography and Anthropology's Cartographic Information Center. The Cartographic Information Center collection contains 125,531 photographs taken between 1931 and 1987 depicting Louisiana. Most of these were taken by the U.S.D.A. or the Louisiana Department of Transportation and Development.

The Map Librarian and Director, John Anderson, permitted the viewing and scanning of aerial photographs taken of Cameron Parish from 1953. Older images dating back to the 1940s are available; however, the study area is not captured in these photos. These images were taken by the Department of Agriculture looking for farmland. Each aerial image is 1:20,000 scale and overlaps individual photos.

2.5.   ArcMap

Each image was scanned and imported in Photoshop. A project in Arcmap incorporates multiple datasets with different datum. The datasets then had to be rectified to the same coordinate system. Many times scanned maps and old aerial photographs are not rectified to a coordinate system, meaning that they are not tied to any specific location on the ground to make use in a geographic information system. When an image does not have a georeferencing system, the software automatically places the image at 0 (degree) latitude and 0 (degree) longitude. North American Datum (NAD) 1927 State Plane Louisiana South Federal Information Processing Standardization (FIPS) 1702 was selected as the coordinate system for the map projection. Map projections are a method in which the curved surface of the earth is portrayed on a flat surface. They are accurately tied to points on the ground and

imported into GIS (Geographical Information System) as a mapping layer. This allows them to be viewed, queried and analyzed along with other geographic data.

The aerial photograph raster image "CJW-3M-48" is used first as the source image. First the aerial photographs files used as the target image need to be in a GIS readable format. .Tiffs, .jpeg, .png, .gifs are acceptable formats while pdfs and .sids are not. The raster image, "Grand Chenier SW," is used as the target image. It contains developed roads to georeference with older aerial photography. These features are ones that will likely be in the source image even if it's sixty years old. This defines the georeference of the coordinate system for the project. Control points are added to tell the source image where to line up with the target image. A minimum of 4 spaced points are used to create an accurate image. Subsequent aerial photographs are then built out and georectified from the initial raster "CJW-3M-48" (Figure 6).
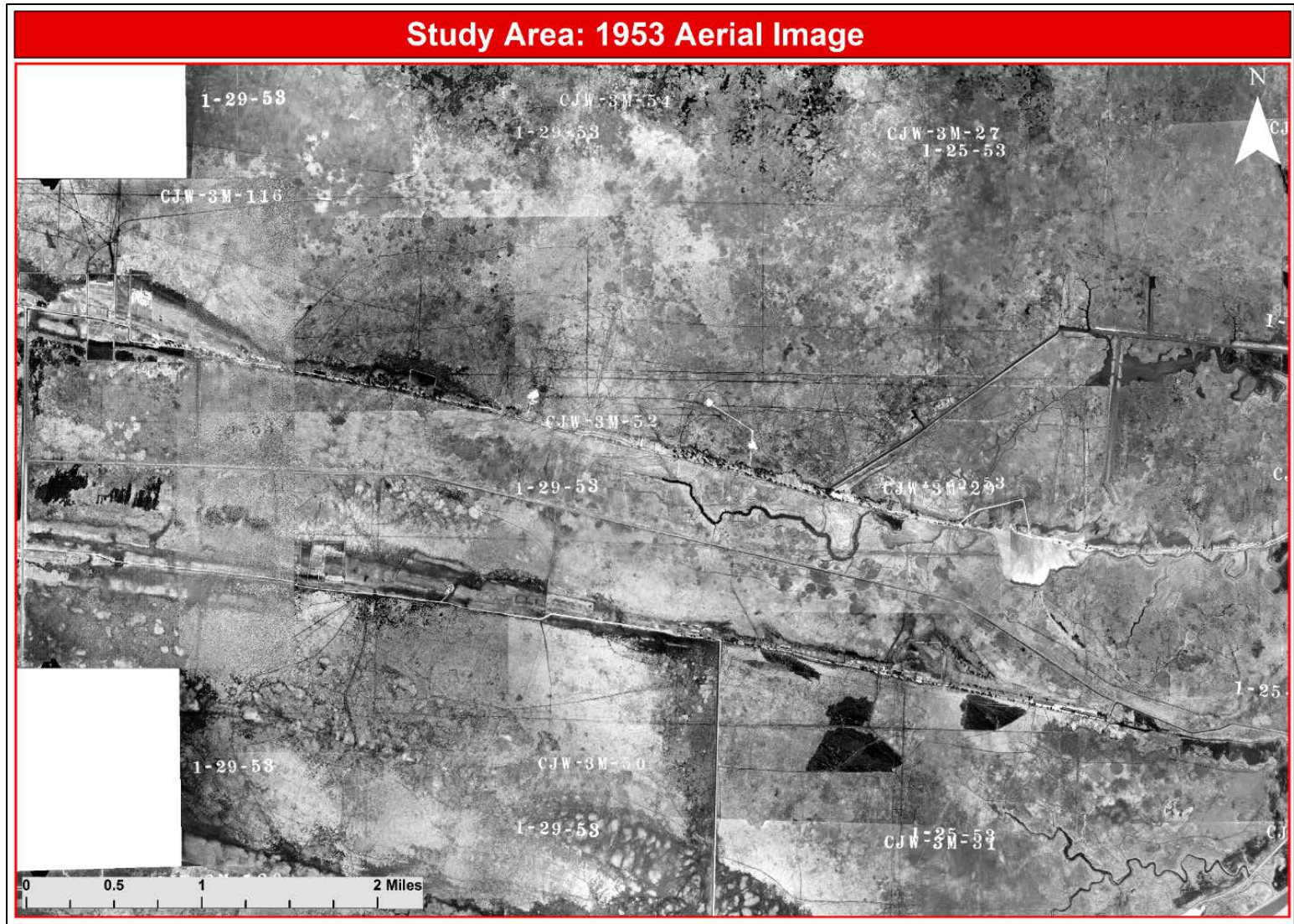
Figure 6: Mosaic of georectified aerial photographs (original image from the LSU Department of Geography and Anthropology's Cartographic Information Center).

3.   Regional Geology

3.1.   Introduction

In the Gulf Coast Region, sediments of the Quaternary period are influenced by various structural features, including but not limited to: salt tectonics, faulting, and subsidence. Both igneous and gravitational activities have played a direct or indirect part with these sediments (Bornhauser, 1958). Generally, sediments have a regional basinward dip, a product of the Gulf of Mexico's geosyncline. This feature plays an interconnected role with many of the influences as mentioned earlier. Typically, younger shallow beds dip a few feet per mile in the Lower Gulf Coastal Plain. In contrast, older and deeper beds can dip up to 200 feet or more per mile (about 2.5°) (Bornhauser, 1958).

3.2.   Tectonics

3.2.1.   Gulf of Mexico Basin.
Beginning in the Late Triassic, the North American plate began to separate from the South American and African plates. These tensional stresses produced subsiding grabens bounded by listric normal faults. As the Gulf's seafloor continued to spread sediments began to infill the accommodation space. These sediments include continental red beds and volcanic deposits that grade into deep and shallow marine deposits (Salvador, 1987). Diabase and basaltic dikes and sills cut thick late Triassic nonmarine red beds but don't penetrate the surface. They have been interpreted to be related to the early rifting of Pangea (May, 1971).

Crustal stretching between the North American and Yucatan block continued through the Middle Jurassic. This crustal stretching was prompted by an oceanic transform boundary, rotating the Yucatan Peninsula block counterclockwise and southward away from the North American plate (Bird et al., 2005). The resultant thinning created a broad depression opening

the central parts of the basin to flooding from the Pacific Ocean (Galloway & Buster, 2011).

It was not until the Callovian (166 Ma) that seawater reached the future Gulf of Mexico

Basin. Sea level changes and thermal activity created conditions favorable for the deposition

of thick Louann salts and evaporites – a defining episode for future structural development of

the Gulf's sedimentary fill. (Salvador, 1987). By 140 Ma, tectonic activity had reached a

state of acquiescence, and the gulf reached its current shape. Subsidence and heavy

sedimentation continue to this day (Salvador, 1987).

3.3.   Salt Tectonics

Throughout most of the northern Gulf region, the Louann salt is deformed into domes,

anticlines, and diapirs that uplift and sometimes penetrate Mesozoic and Cenozoic strata

(Martin, 1978). Numerous oil and gas fields along the Gulf Coast, specifically South

Louisiana, are influenced by the movement of this salt (Bearb, 2013). Salt migration affects

the transport and deposition of sediments and can form a wide range of hydrocarbon traps.

In southern Louisiana, the Louann salt is the primary source of diapiric salt (Antonie and

Bryant, 1969) The Louann salt is divided into three prominent belts based on salt

morphology and accumulations (Martin, 1978): (1) the inner belt consists of Mississippi,

Louisiana, East Texas, and South Texas salt basins featuring small isolated diapirs and deep-

seated anticlinal swells; (2) large, isolated diapiric stocks and expansive anticlinal swells

occupy a middle belt containing the Louisiana-Texas coastal and inner shelf salt domes; (3)

an outer belt that includes all of the continental shelf and slope from DeSoto Canyon to

northern Mexico is characterized by very broad, nearly continuous ridge-like massifs and salt

tongues (Figure 8).

Salt domes located in these three belts can be broken down further into localized structures. Salt domes can be responsible for creating a range of complex structures in the subsurface. Many of these features include growth faults, graben faulting, radial faulting, and salt withdrawal (Ocamb, 1961). Growth faults are probably the most distinctive feature of southern Louisiana geology (Thorsen, 1963). Growth faults are believed to be caused by penecontemporaneous fault movement and sediment loading. This movement is often attributed to deposition on the underlying Louann salt which initiated flowage on the salt and slope mud, thus leading to the development of growth faults (Bruce 1973).
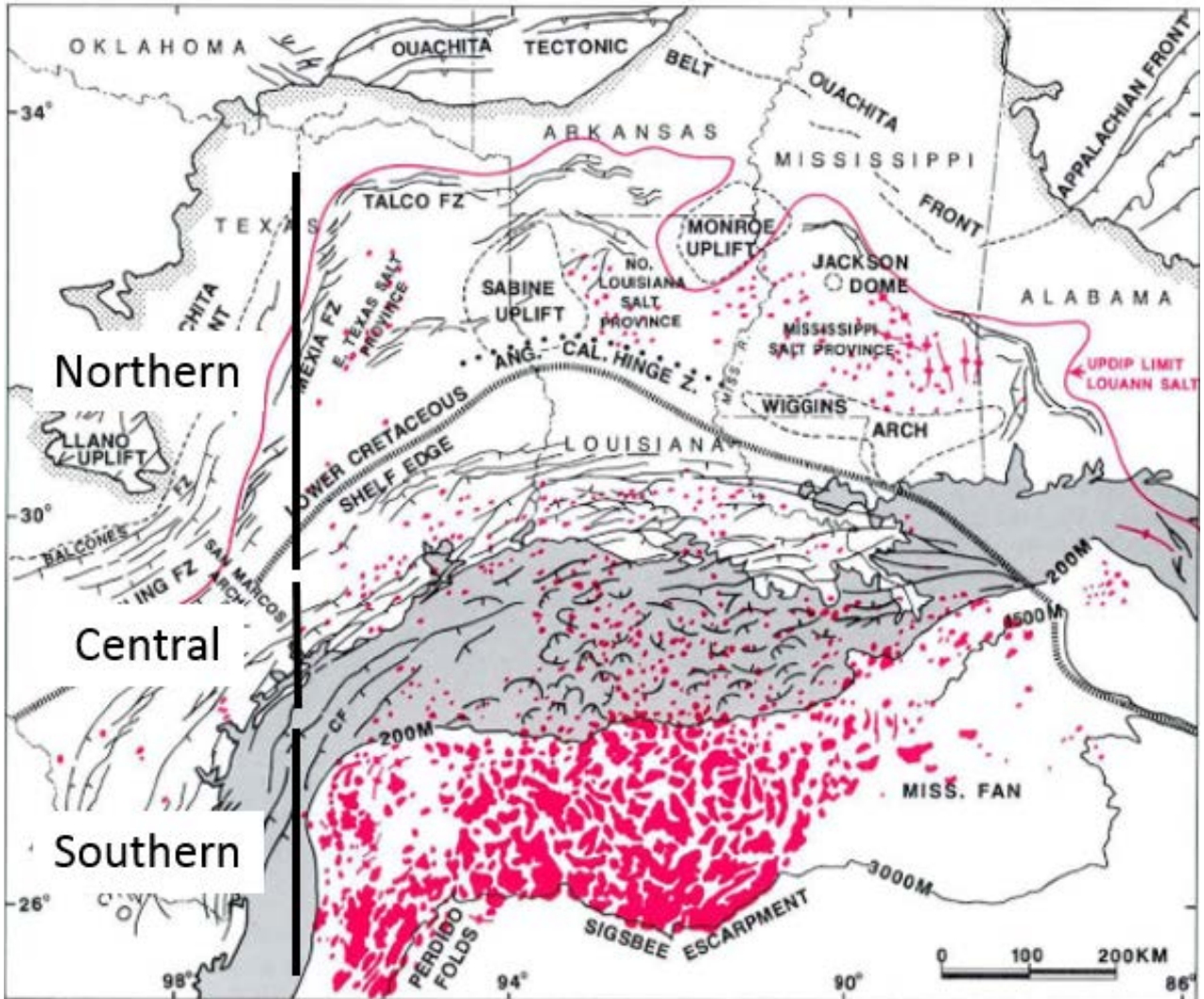
Figure 7: Tectonic map of northwestern Gulf of Mexico. Study area lies south of Lower Cretaceous shelf edge. Black lines are normal faults. Salt features are shown in red based on R. G. Martin (1978) work. Continental shelf is shown in gray. Modified from Worrall and Snelson (1989).

3.4.   Gulf Coast Faulting

The dominant structural features of Cameron Parish are sizeable down-to-the-south growth faults and include, to a lesser extent, piercement-type salt domes, deep-seated domes, and other fault structures (McLean, 1957). The Gulf Coast's relationship with faulting is derived from sediment loading on ancient unstable Late Cretaceous shelf margins (Yang et al., 1992). Throughout the Cenozoic sedimentation surpassed the rate of subsidence such that there was a seaward shift of depocenters and shelf edge progradation toward the basin (Yang et al., 1992). Increased sediment loading on the earlier deposited Louann salt is thought to have initiated movement of the salt and slope mud, contributing to the development of growth-faults (Bruce, 1973). Growth faults generally have an east-west trending strike parallel to sub-parallel with the shoreline of the Louisiana Gulf Coast. Deformation and migration of salt influences the movement of growth faults providing accommodation for deposition on the downthrown side. This accommodation plays an integral part with growth faults. Strata downthrown tend to dip into the created space forming "rollover" anticlines (Figure 9). A contemporaneous interaction between deposition and displacement that defines growth faults. These faults are further characterized by a substantial increase in throw with depth and across which, from the upthrown to downthrown block, there exists considerable thickening of correlative section. Faults associated with Gulf Coast geology can be growth or non-growth faults, both of which are commonly characterized by medium-angle dips (Ocamb, 1961).

These types of normal faults can trend regionally or can occur in isolated localities. Displacements can range from tens to several hundreds of feet (Ocamb, 1961). Most South Louisiana faults increase in throw with depth. The displacement of growth faults can exceed 3000 ft in some instances (Tearpock, 1991). They are typically a medium angle fault (40° to

60° dip), with typically a 45° dip in the Gulf Coast basin, but tend to broaden with depth
(Ocamb, 1961). Low angle faults (dip less than 40°), while rare, are mostly associated with
domes of the Oligocene and Miocene trends. Faults with high angles of dip (dip greater than
60°), are relatively common in the subsurface of Louisiana and typically occur around
piercement salt domes (Ocamb, 1961). The majority of faults decrease in dip with depth.
Other features associated with faulting typical of the Gulf Coast include synthetic or
antithetic secondary faulting. Synthetic faults develop along strike and have the same
direction of dip as their parent fault. Antithetic faults dip the opposite way of their parent
fault while maintaining a parallel strike. Splinter faults can also develop from their parent
fault. The total throw of two or more regionally developed growth faults resulting from the
parent split usually equals the throw of the parent fault (Ocamb, 1961).
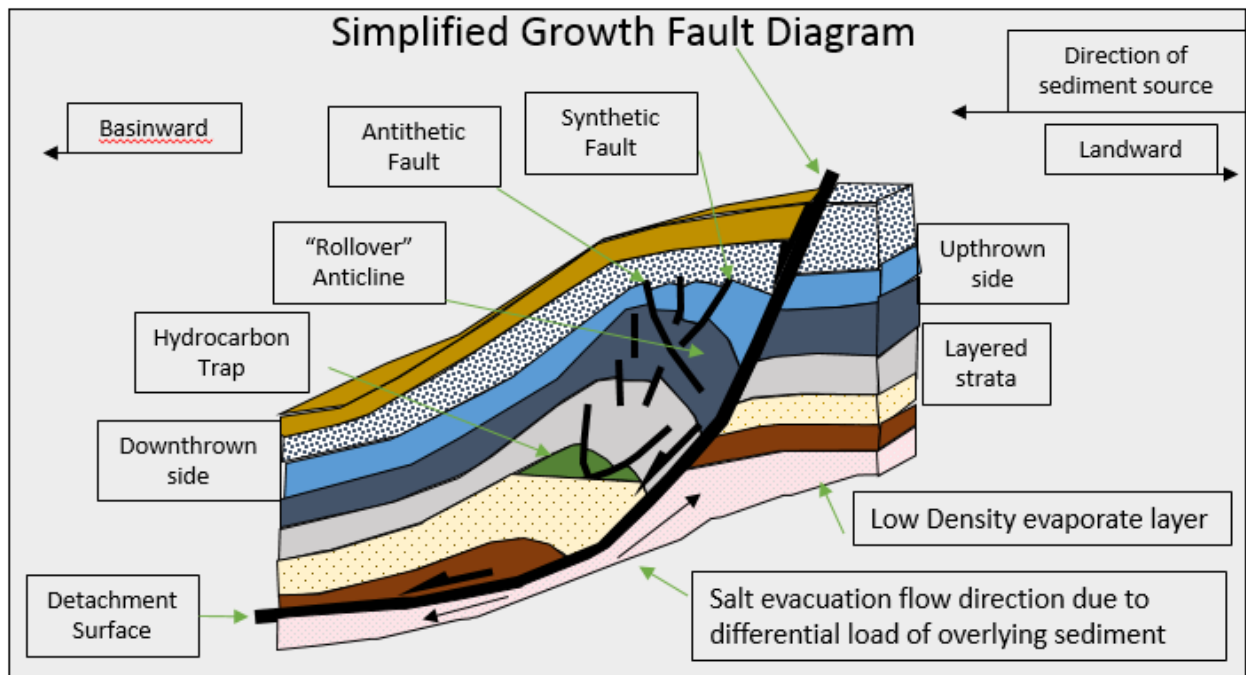
Figure 8: Growth fault diagram (O'Leary, 2018 modified from Emadelfar, 2013)

3.5.   Subsidence

Subsidence is the gradual sinking of an area of land, with respect to some geodetic level (sea level for example). It can result from natural and/or anthropogenic processes. Natural sources of subsidence include compaction and consolidation, faulting, sediment diagenesis, and tectonic loading (Gagliano, 2003). Anthropogenic actions associated with subsidence include groundwater withdrawal (Dokka, 2011). In the study area, the combination of sea level fluctuations, reduced sediment supply, wave action, compaction and consolidation of sediment through dewatering controls the subsidence of the Chenier Plains (Gosselink et al., 1979). Compaction and consolidation play a dominant role. These processes include, for example, consolidation of sediment textural variability; compaction of underlying sediments from weight of levees (both natural and artificial), beaches, building, piles and fills; lowering of the water table through extraction of groundwater, salt, sulfur, oil, or gas, or reclamation practices; and extended droughts or marsh burning that cause surface dehydration and shrinkage in highly organic soils (Gosselink et al., 1979).

Some studies attribute subsidence to compaction of Holocene sediments, and argue that the Louisiana coast is stable in a "vertical" sense and restoration efforts will offset the natural compaction of Holocene sediments (Törnqvist et al., 2006; González and Törnqvist, 2006). However, recent studies performed in the Mississippi River delta plain suggest that subsidence affects not just Holocene sediments but extend deeper to the Pleistocene sediments (Dokka, 2011). In the Chenier Plains, the Pleistocene surface lies only 33 ft below the surface while the Mississippi River Delta's Pleistocene surface is 984 ft deep (Fisk and McFarlan, 1955). In the past, Gosselink et al. (1979) found that the overall net rate of subsidence (or relative sea level rise) averages 0.69 in/year on the Chenier Plain. Recently,

using data from the Coastwide Reference Monitoring System (CRMS), Nienhuis et al. (2017)

found subsidence rates have reduced to 0.35 in/year in the Chenier Plain based on shallow

subsidence rates by taking the difference between vertical accretion of sediment and surface-

elevation change (Figure 9).
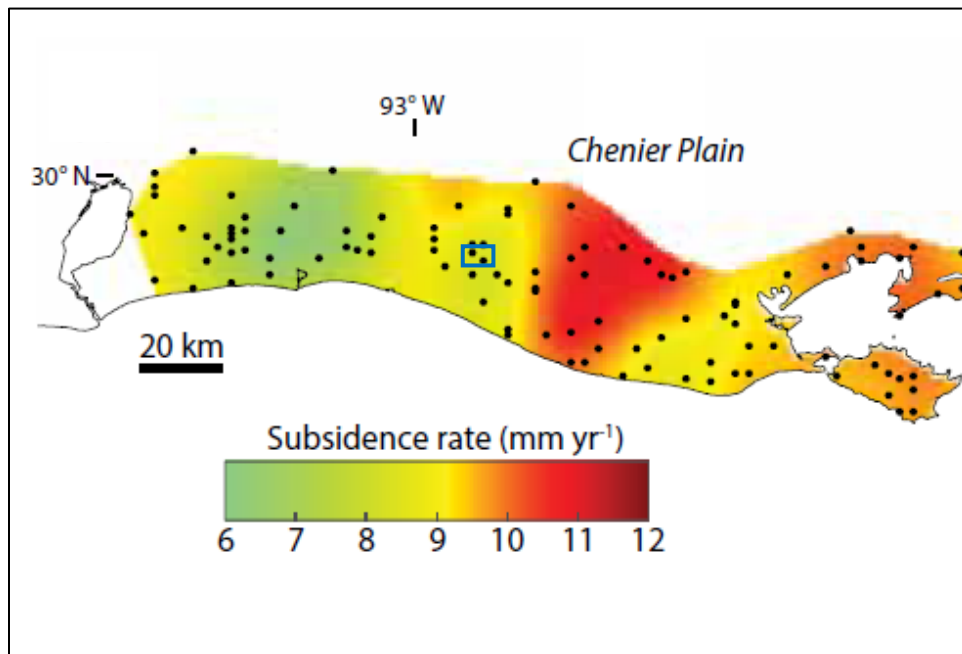
Figure 9: Subsidence map for coastal Louisiana based on geostatistical interpolation (kriging) of CRMS data (black dots) of land-surface subsidence rates over the past 6-10 years. Blue box indicates the study area. Modified from Nienhuis et al. (2017).

3.5.1. Growth faulting related to subsidence. While consolidation and compaction is responsible for subsidence within Holocene sediments, deeper processes such as growth faulting can also contribute (Dokka, 2006). Growth faults propagate upward through thin sedimentary cover (Kuecher, 1995). Kuecher (1994) interpreted seismic sections illustrating evidence of subcropping faults in the Lafourche Delta. These faults, the Golden Meadow and Lake Hatch faults, have been located on seismic surveys, as well as concluded to be active in the Holocene sedimentary section based on core data on both sides of the fault (Kuecher, 1994). In some areas of South Louisiana, subcropping growth faults have a causal relationship with new areas of land loss (Kuecher, 1994). Studies conducted by Dokka (2011) have shown active faulting displacements of the Tepatate-Baton Rouge and Lake Ponchartrain fault systems by 2.5-5 cm between 1990 and 1996 and 7.5-10 cm 1986-1996, respectively.

Furthermore, faulting can contribute to tectonic subsidence – the sinking of Earth's crust. Through geodetic leveling and water gauge observations, Dokka (2006) found tectonic subsidence accounted for 73% of total subsidence in the Michoud area of Orleans Parish, Louisiana. Between 1969 and 1971, benchmarks in the hanging wall of the study area showed 0.39 cm/year of subsidence and 0.23 cm/year from 1971 to 1977. This happened to coincide with activation of the Michoud fault which slipped 0.24 cm/year from 1959 to 1971 and 0.15 cm/year from 1971 to 1977. Measurements were made with respect to the reference datum, North American Vertical Datum 88 (NAVD88).

Quaternary faulting along the Gulf Coast have also been document in Texas. Verbeek (1981) recognized a strong connection between subsurface and surface faulting in Houston based on seismic data, aerial photos from the 1930s, topographic maps, well log surveys, and structure

maps (Verbeek et al., 1981). Increased stratigraphic separation with depth suggests that faults re-initiated today were also active during contemporaneous Pleistocene sedimentation. Shallow Tertiary growth faults cut overlying Pleistocene sediments and are known to exhibit scarps at the surface. Sequential aerial photographs show faulting over the last several decades. Both natural forces and anthropogenic activity may prompt the faulting, which ranges in vertical separation of 0.5 to 2 cm/yr (Verbeek et al., 1981). Local uplift associated with salt domes, diapiric shale, differential compaction and gulfward creep of sediments are all natural, though unlikely, causes of faulting (Verbeek et al., 1981). Extraction of hydrocarbons and groundwater has been suggested to have accelerated, or at least re-initiate the faulting (Verbeek et al., 1981). Active faults are more prevalent in areas where the demand for groundwater is greater. However whether differential compaction of aquifer sediments related to withdrawal or ground-water withdrawal itself is the cause of faulting remains to be understood (Verbeek et al, 1981).

3.6.   Geologic History of Chenier Plain/Sedimentary Environment

The Northern Gulf of Mexico Basin is composed of sediments deposited by several Louisiana distributaries – branches of a river, including the Mississippi and Atchafalaya rivers. The counterclockwise nature of the Gulf of Mexico's marine circulation reworks and disperses these delta sediments westward across the coast of Louisiana and Texas (Nevitt, 2017). These sediments are the primary source that contributed to the formation of Chenier Plain's paleo-beaches reworked by wave and storm energy (Gosselink et al., 1979). Bay, lake, and marsh deposits, situated both vertically and laterally to each other, are among other sedimentary environments comprising the Chenier Plain (Gosselink et al., 1979). Environments that were once a coastal marsh could quickly become a lake or bay in

relatively short intervals of time due to minute changes in rates of sea level rise and subsidence (Figure 10 & 11, Gosselink et al., 1979). Radiocarbon content of marsh deposits can be used to reconstruct the depositional histories and rates of subsidence of these areas (Gould and McFarlan, 1959; Dokka, 2006). These near surface deposits rest upon a seaward-thickening accumulation of gulf-bottom sands and silty clays that comprise the upper part of the sedimentary wedge (Gosselink et al., 1979) (Figure 10 & 11). These deposits are identified by marine fauna, unique sedimentary structures, and absence of organic detritus accumulations. Bay and lake deposits can be distinguished from each other mainly in their exposure to varying degrees of river and tidal influence (Gosselink et al., 1979). Drowning of relict Pleistocene entrenched valleys formed many of the inland water bodies, for example, East Bay, Sabine Lake, and Calcasieu Lake along the coast, and Grand Lake and White Lake located inland from major Gulf connections. Most of the small lakes originated as marsh ponds that enlarged from subsurface or salinity changes that altered the marsh-building process (Gosselink et al., 1979). Irregularly shaped lakes typically represent abandoned river or tidal stream courses (Gosselink et al., 1979).

3.6.1. Chenier Plain Formation. The formation of the Chenier Plain stabilized around 3,000 years ago as global sea level rose to its present day level. The Chenier Plain is situated to the south of the coastal prairie region on the coast and spans from Vermilion Bay to Galveston Bay in Texas. To the North, Pleistocene-aged deposits, which form the geologic substrate and upland prairie region of the Chenier Plain region, are found a few kilometers inland from the coast and dip gently into the continental shelf's slope. The formation of the Chenier Plain is directly related to the nature of the Mississippi River's delta lobe switching (Figure 12). When the distributary system was more westward, sediment influx was high, and the shore shifted seaward. When the river took a more eastwardly course, erosive wave action reworked sediment into high beach ridges (Figure 11). Chenier Plains are thought to have formed by this alternation of suspended sediment deposition and wave erosion of sandy mud, leaving winnowed sand and shells behind (Figure 12) (Howe et al., 1935, Russell and Howe, 1935). Extension of the cheniers occur in areas not actively eroding. Moderate storm surges may build up several meter high chenier while severe storms urges may wash over active cheniers – producing washover sand deposits accompanying eroded shoreface/dunes. Gould and McFarlan (1959) reconstructed the history of the Chenier Plain through the use of aerial photo mosaics, topographic maps, boring and physiographic analysis of the Chenier Plain along with radiocarbon dating to establish geochronology. In the absence of wood and peat, the delicate Mulina shells were used to date samples (Gould and McFarlan, 1959). A wedge of relatively recent sediments recorded the final post-glacial sea level rise and present-day deposits. Progradational Chenier Plain deposits compose the upper part while the basal wedge consists of sediments deposited during a transgressive stage as the sea advanced across the entrenched and subaerial Pleistocene Prairie Terrace (Gould and McFarlan, 1959).

Thin organic clays and peat from this basal unit, which date back to 5600 years ago, rest unconformably on the Prairie Terrace. This underlying Pleistocene Prairie Terrace consists of deposits that exceed the radiocarbon dating and therefore are "over 37,000 year old" (Fisk and McFarlan, 1955). Deposition of silty strands and gulf bottom sands and silts topped by brackish marsh and bay deposits signaled the end of transgression and beginning of progradation (Gould and McFarlan, 1959). When the Mississippi River held a more westerly course during the Teche sub-delta phase 3800 – 2800 BP, mudflats prograded north of the earliest Chenier Plain shoreline. Outbuilding ceased around 2800 BP when the Mississippi River favored the eastward St. Bernard delta complex, reducing the sediment supply. Gould and McFarlan (1959) – noted Pecan Island and Little Chenier are remnants of the first shorelines formed during this period of stability and are the oldest cheniers. Worn conditions of shells and microfauna are evidence of this period's strong wave activity (Gould and McFarlan, 1959). Around 1200 years ago the delta switched to the Lafourche outlet, providing a considerable sediment influx for the Chenier Plain to continue seaward with additional input from Plaquemines and modern-day outlet. Changes within the Lafourche delta lobe and temporary distribution through the Plaquemine-Belize (birdsfoot) delta lobe created the majority of the chenier's geomorphology (Gould and McFarlan, 1959; Penland and Suter, 1989; McBride et al., 2007). By 300 years BP the Lafourche delta lobe was completely inactive, the Mississippi River's course switching to the Plaquemine delta, allowing erosive forces to dominate the Chenier Plain coastline once again.
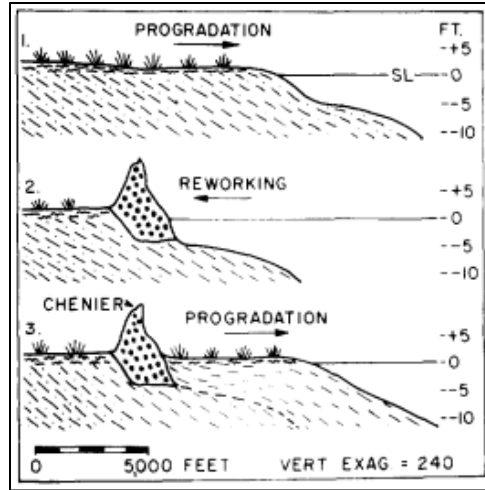
Figure 10: Hoyt's (1969) Chenier Plain process idealized cross section model. 1. Mudflat progradation. 2. Erosion and reworking of mudflat deposits and formation of ridge along shoreline. 3. Mudflat progradation, ridge becomes Chenier. SL = seal level
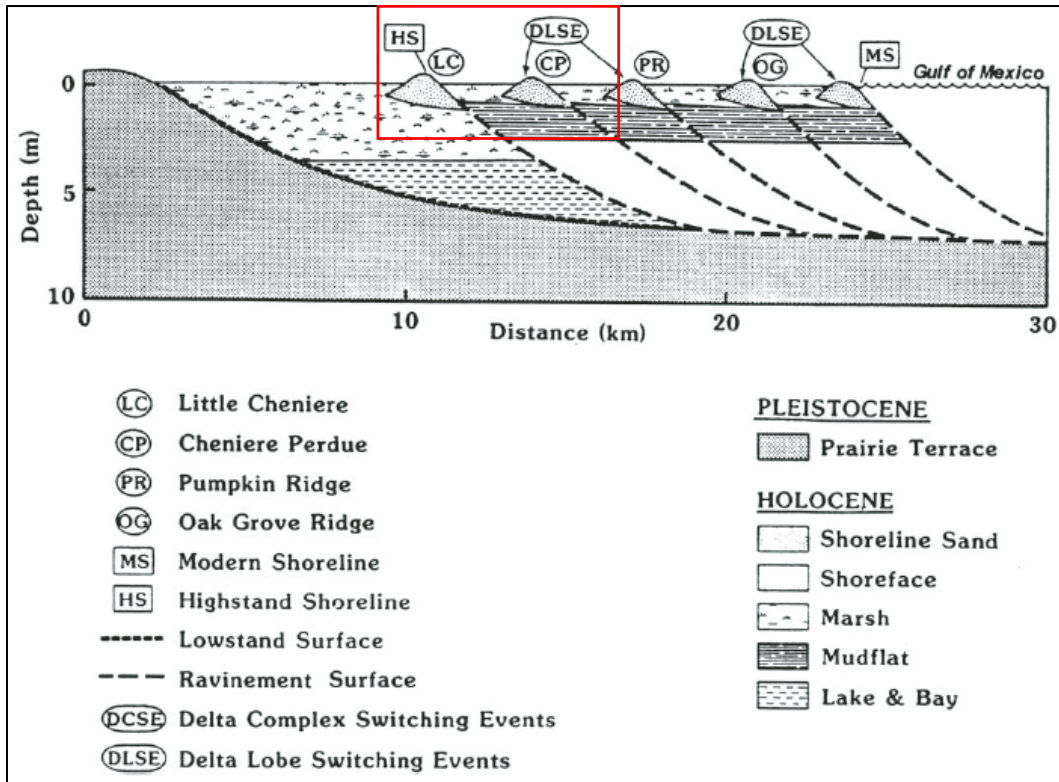
Figure 11: Idealized cross section across Chenier Plain with chronostratigraphic interpretations of facies belts. cheniers become younger from landward (left) to seaward (right). Red box indicates cheniers in Study Area. Modified Owen (2008) from Penland and Suter (1989)
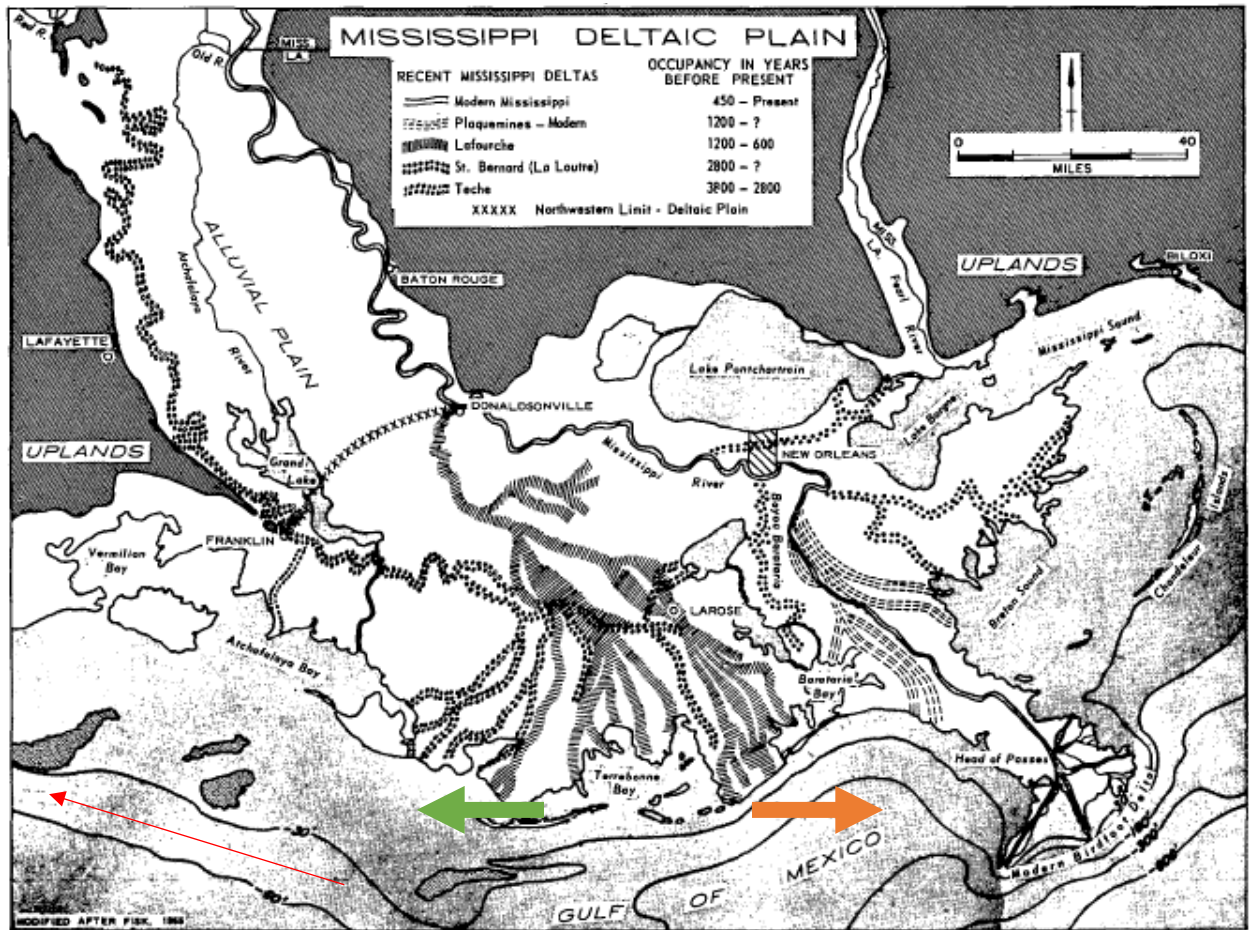
Figure 12: The Mississippi Deltaic plain showing recent subdeltas and associated river and distributary courses. Arrow (red) indicates direction of longshore drift. Impact of delta lobe switching indicated by Green (left) signifies higher sediment influx – shore shifts seaward. Orange (right) reduced sediment influx – erosive wave action, cheniers form. Modified Gould and McFarlan (1959) from Fisk (1955)

3.6.2. Internal stratigraphy of Chenier Plain.

The Chenier Plain is comprised of offshore mud and a shallow marine fauna with silty clay covered by shallow marine silty clay series of mudflats compose a regressive sea cycle. Transgressive sand with reworked shallow marine and brackish shell fauna follows, and is topped by Coastal dune and sandstone with root structures and possible marsh paleosol (Figure 10). Chenier is derived from the Cajun word for "live oak", which is the primary tree species dominating the crest of ridges. The Chenier Plain itself extends laterally 200 km from Sabine pass, Texas to Vermilion Bay of Louisiana, varying in width between 20 and 30 km with elevations approaching 8 m on the ridges. The Mermentau, Calcasieu, and Sabine rivers incise distributaries throughout the complex. Their lakes, Calcasieu and Sabine Lake, dominate the western landscape while Grand and White Lake occupy the eastern area of the Chenier Complex. Five major sets of Chenier Ridges thicken seaward between 6 and 8 m and are separated by prograding mudflats. These prograding mudflats results from periodic pulses in sediment delivery as the Mississippi River Delta shifted westerly. Stratigraphically, this vast complex can be broken down into distinct cheniers, beach ridges, Mudflats, and recurved spits. The facies accompanying the plain reflect that of a beach Ridge. They typically are on the updrift side of a distributary and intercept sediments transported by longshore currents. These coarsen upwards from fine grained silt and have foreshore and wash over deposits commonly accompanying their crest. At the base, bioturbation of massive silty sands is common and becomes less prevalent upward. Detrital shells and organic fragments are common. Tropical and winter storms may deposit sand sheets on the shore face or inner shelf. A major progradation during the late Holocene (3000 – 4000 years ago) prompted the formation of Little Chenier and Pecan Island. These represent the maximum flooding shoreline of the

Lafourche delta. The formation of cheniers more closely match in time with individual switching of Lafourche delta lobes than the switching of delta complexes.

3.7. Natural and Anthropogenic Activity

3.7.1. Hurricane impact.

In recent history, the Chenier Plain has been affected by several major storms that have shaped its landscape. High energy storms and less frequent, but nonetheless powerful, tropical cyclones contribute to Louisiana's sediment budget. Hurricanes rework offshore sediments and widely redistribute them across Louisiana's Deltaic and Chenier Plains. Winds push water into a storm surge occupying an area greatest in the northeastern quadrant of the storm. As hurricanes approach, their intensity, trajectory, speed and sediment availability affect the amount of sediment deposited on the marsh during the storm surge (Cahoon et al., 1995; Nyman et al., 1995; Nevitt, 2017). The last major hurricane to impact the northwestern Gulf of Mexico coastline was Hurricane Rita in 2005. Its storm surge reached a record height of nearly 17 ft (Turner et al, 2006). Hurricane Rita made landfall on the Louisiana-Texas border, blowing the highest surge, on the northeast side, over Grand Chenier. On average, hurricanes move and redeposit 5.6 million metric tons of inorganic sediment a year, roughly 4% of the modern Mississippi River sediment load (Tweel and Turner, 2014). In severe storms, sediment deposition can be far greater than average. For example, Hurricane Rita resulted in 48 million metric tons of sediment deposition over coastal wetlands (Tweel and Turner, 2012). This redistribution of Mississippi River sediments from offshore is an integral portion of Louisiana's sediment budget.

Despite popular belief, most inorganic/mineral sediment in Louisiana coastal wetlands appears to come from hurricanes. Most organic material, which is the majority of wetland volume, is produced on site through wetland processes. It is true that there are land losses

32

from hurricanes, but these are largely lateral (edge erosion) rather than vertical (surface elevation loss). Hurricanes bring in massive quantities of sediments that are deposited in a broad blanket.

3.7.2. Hydrologic history. The study area lies within the Mermentau River Basin, specifically the Lakes Sub-Basin (Figure 13). This basin is located in the eastern portion of the Chenier Plain. It straddles Cameron and Vermilion Parishes and comprises 450,000 acres of marsh. This marshland is made up of 190,000 acres of Fresh Marsh, 135,000 acres of Intermediate Marsh, and 101,000 acres of brackish marsh (Coastal Wetlands Planning, Protection and Restoration Act – CWPPRA, 1999). Flood control and navigation projects on the Mississippi River and Atchafalaya River restrict natural process to small areas. Prior to this restriction, these rivers added sediments necessary for marsh building to the region. Consequently, marsh building only occurs on the eastern flank of Mermentau Basin's coastline. Sea level rise, approximately 0.25 in/year, and subsidence further aggravate this issue (CWPPRA, 1999). Vegetation degradation and regeneration normally maintains wetlands; however human alterations have jeopardized this system. Flooding is a major problem in the lakes sub-basin. Highway 82 and Highway 27 to the south and to the west of Grand Lake, respectively, increase ponding and block drainage to the adjacent Calcasieu/Sabine basin and southern Chenier sub-basin. The Catfish control point Grand Lake, controls the major drainage outlet from the Mermentau River in the Lakes sub-basin to the Chenier sub basin. This structure was built to reduce saltwater intrusion into Grand Lake but also limits the outflow of freshwater to the marsh. Normally, this impounded freshwater would reach the Chenier sub-basin to the south but highway 82, which connects Grand Chenier and Pecan Island, prevents this. It functions as a dam, which prevents fresh water outflow, but also serves as a levee to prevent the inflow of salt water. However when overtopped by a hurricane's storm surge, salt water will pond and cause damage to the marsh. The ebb and flow of fresh versus salt water is a tidal effect that has been disrupted by

man-made structures. This excessive flooding is the most critical problem. Prolonged high-water leads to vegetation change and wetland loss. These high salt water levels cause erosion on lake rims which protect interior fragile marsh. Erosion is accelerated when this vegetation is gone.
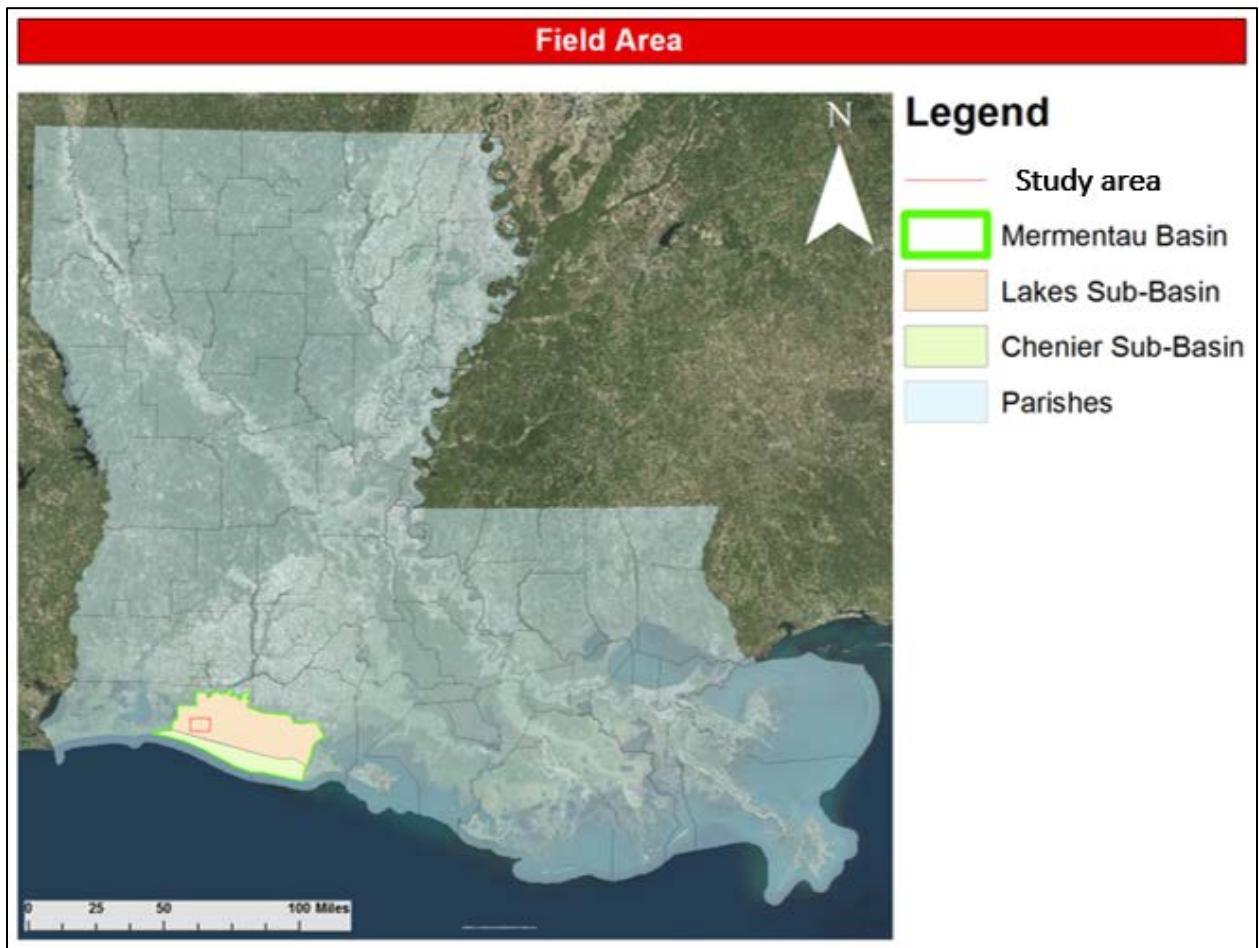
Figure 13: Hydrologic Basin of the study area.

4. Results

4.1. Description of the faults in the subsurface from the seismic survey

A detailed analysis of the seismic survey revealed the presence of 10 fault surfaces, labeled A-J (Figure 14). Faults are picked from west to east based on visible offset between horizons. Faults were picked from the bottom up, to the shallowest interpretable time horizon. Faults were projected to the surface, maintaining constant dip. An error pick was made on the western, central, and eastern portions of the fault as well as a recording of the steepest or shallowest reach of fault picks, defined as ε^- and ε^+, respectively (see Figure 15), thereby defining a "dip uncertainty window". This dip uncertainty window was also projected to the surface, and was determined to be an average of approximately $\pm$ 400 ft in radius (see Figure 15). This error was based on the distance between the last pick of confidence angle used to extrapolate the fault surface and zero. Fault surfaces were converted from time to depth, subsea (Table 1). Four horizons were picked between 3500 and 5000 ft on the central portion of each fault. Horizons were unique to each fault and were picked on strong reflectors. The difference in downthrown interval thickness of downthrown fault was divided by the difference in upthrown interval thickness for three expansion indexes - shallow, intermediate, and deep for each fault.

In summary, all Faults are high angle normal faults. Fault A and C have a northeast-southwest strike and while all other fault strike east-west. Faults A-C dip to the south, while faults D-J all dip to the north, forming a graben in the center of the study area (Table 2, Figure 14, 16, 17).
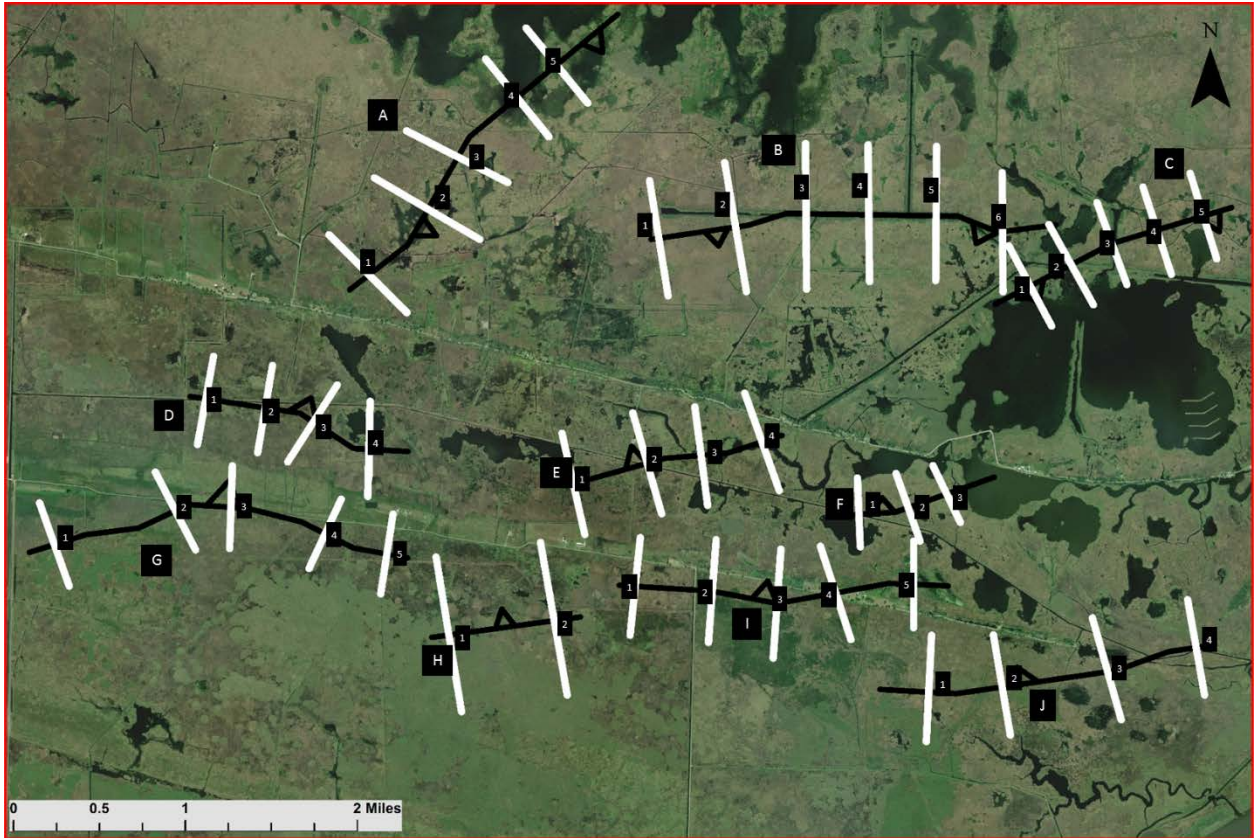
Figure 14: Ten faults were discovered in the study area (red lines labeled A-J). All faults are normal; red triangles denote the downthrown side (footwall). Fault offset was investigated along transect perpendicular to each fault (yellow lines).

Table 1: Time depth conversion chart.

Fault	Depth (ft) and (s)					
	East		Central		West	
A (Top)	-2100	0.613	-1040	0.296	-1710	0.492
A (Bottom)	-10800	2.688	-8980	2.296	-10610	2.625
B (Top)	-1840	0.530	-1450	0.416	-2300	0.676
B (Bottom)	-6300	1.724	-6500	1.766	-8600	2.227
C (Top)	-1690	0.482	-3177	0.539	-1470	0.417
C (Bottom)	-7100	1.934	-9150	2.327	-8800	2.267
D (Top)	-2270	0.655	-2150	0.622	-2750	0.800
D (Bottom)	-3930	1.125	-4860	1.381	-5975	1.667
E (Top)	-2210	0.589	-1730	0.488	-1920	0.556
E (Bottom)	-7140	1.95	-6440	1.748	-5065	1.435
F (Top)	-2002	0.578	-1793	0.514	-1713	0.493
F (Bottom)	-6560	1.780	-6865	1.850	-4938	1.405
G (Top)	-2030	0.592	-2140	0.622	-2600	0.74
G (Bottom)	-10571	2.617	-9230	2.317	-9400	2.378
H (Top)	-1700	0.486	-1630	0.467	-2035	0.597
H (Bottom)	-8920	2.275	-8980	2.308	-9120	2.322
I (Top)	-1630	0.468	-1540	0.422	-2500	0.698
I (Bottom)	-9490	2.398	-8787	2.258	-7005	1.862
J (Top)	-2463	0.629	-1079	0.526	-2075	0.535
J (Bottom)	-8610	2.219	-9140	2.232	-8900	2.221
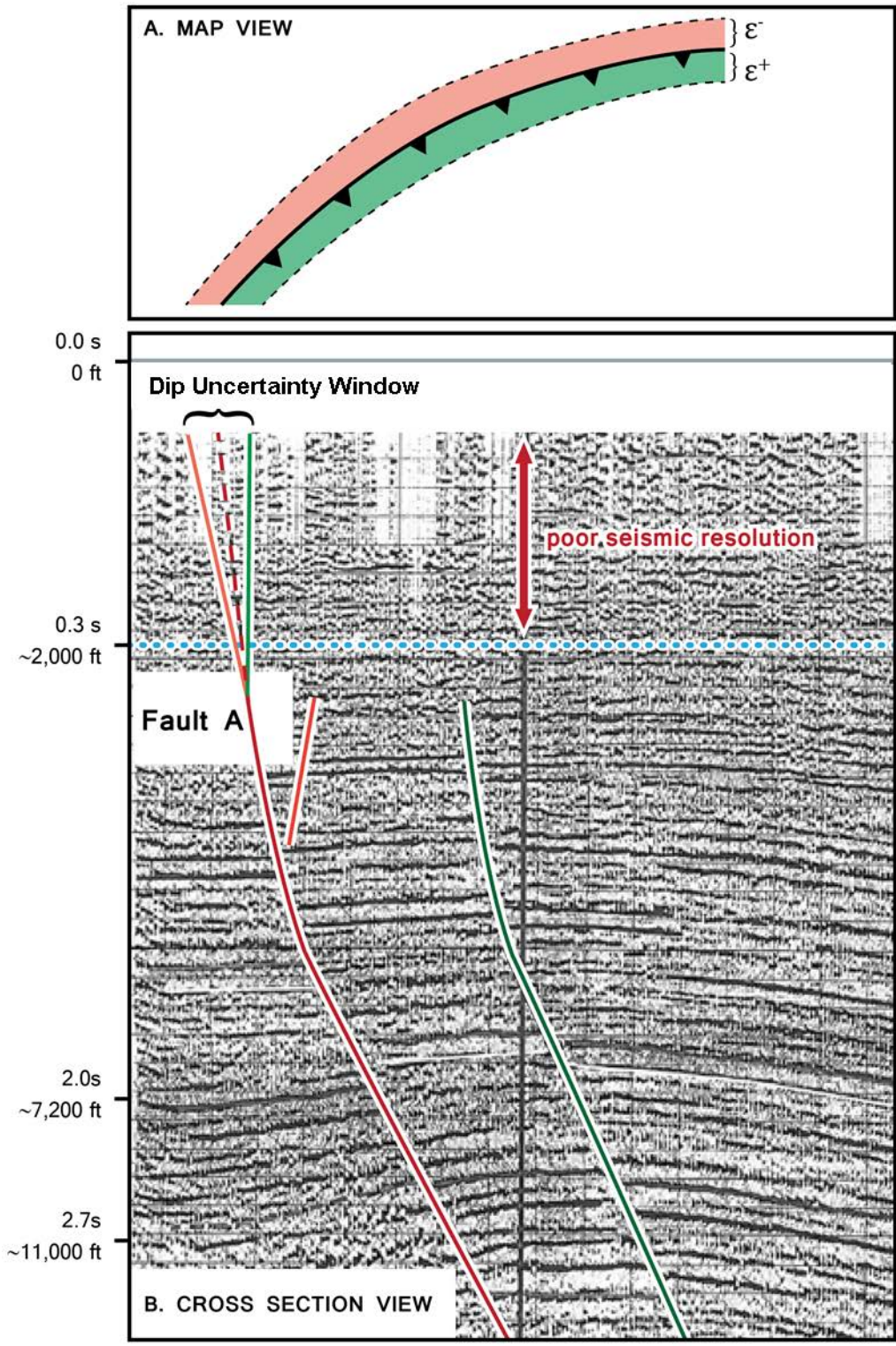
Figure 15: Example of fault in seismic data. Faults are picked as shallow as the seismic resolution allows it. The fault trace is then projected to the surface maintaining constant dip, and the fault can be trace don a map view. However, the dip of the fault falls within a "dip uncertainty window", which, when projected in map view, defines two error measurements: the error on the upthrown (ε^-) and downthrown side (ε^+) of the fault, respectively. Figure Seismic slice adapted from Martin (2006), not to scale, use as reference only.

40
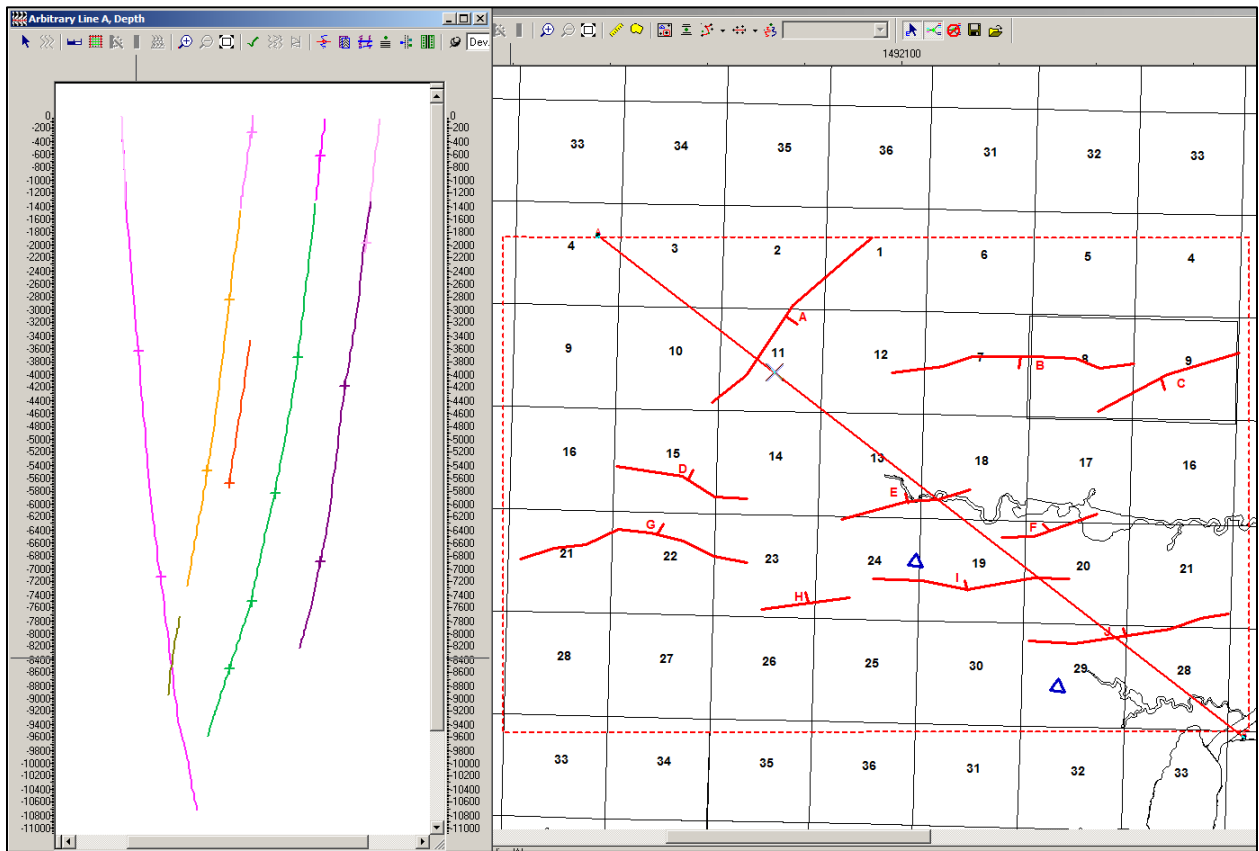
Figure 16: Arbitrary northwest (left) southeast (right) line. Fault A (pink) dips to south. Fault E (gold), Fault I (green), and Fault J (purple) dip to the north. Pink extensions are extrapolation picks. Blue triangles location of wells with electric logs.
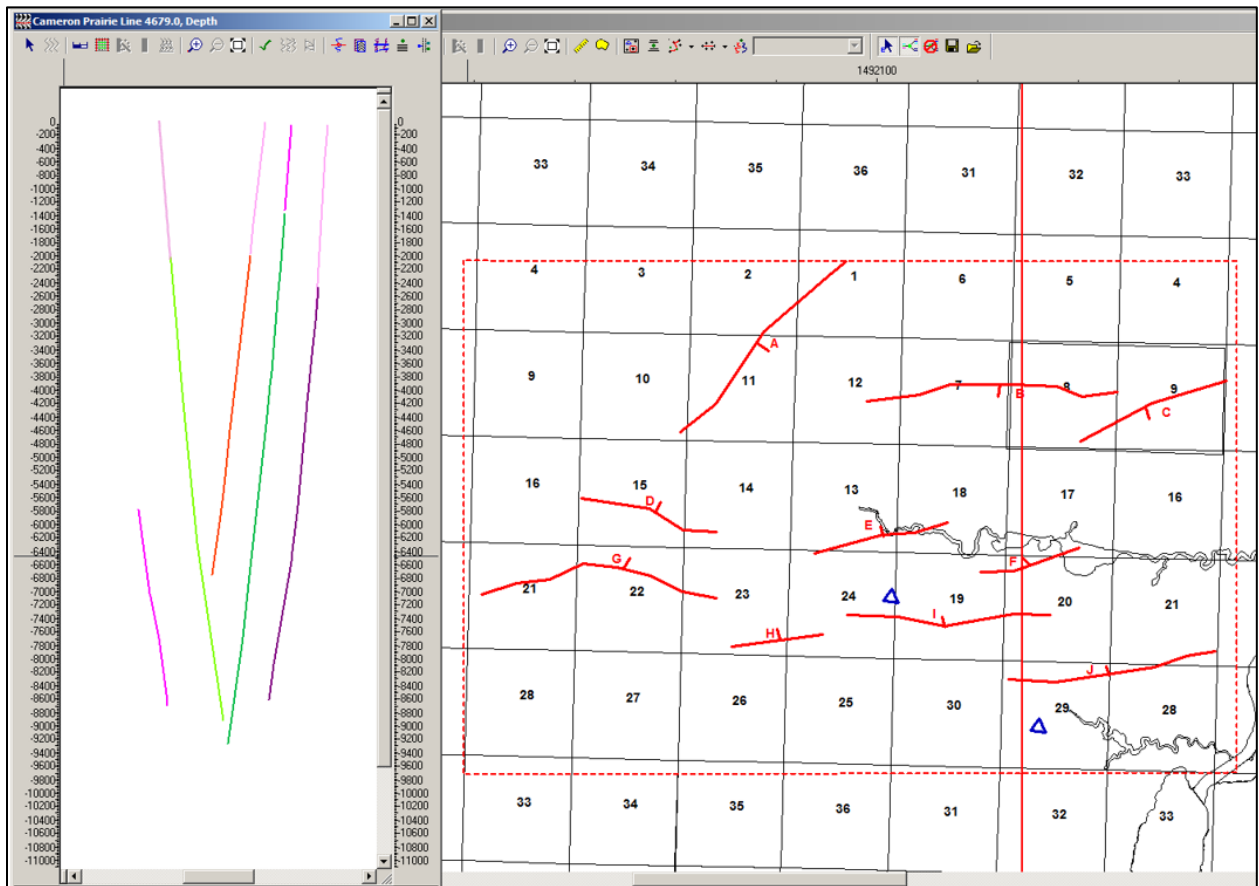
Figure 17: North (left) south (right) inline. Fault B (lime green) dips to the south. Fault F (orange), Fault I (green), and Fault J (purple) dip to the north. Pink extensions are extrapolation picks. Blue triangles location of wells with electric logs.

Table 2: Fault depths and "Dip Uncertainty Window" error

Fault	Depth (ft)			Error ε⁻ (ft)	Error ε⁺ (ft)
	East	Central	West		
A (Top)	-2100	-1040	-1710	395	189
A (Bottom)	-10800	-8980	-10610		
B (Top)	-1840	-1450	-2300	357	287
B (Bottom)	-6300	-6500	-8600		
C (Top)	-1690	-3177	-1470	434	209
C (Bottom)	-7100	-9150	-8800		
D (Top)	-2270	-2150	-2750	605	314
D (Bottom)	-3930	-4860	-5975		
E (Top)	-2210	-1730	-1920	532	446
E (Bottom)	-7140	-6440	-5065		
F (Top)	-2002	-1793	-1713	370	200
F (Bottom)	-6560	-6865	-4938		
G (Top)	-2030	-2140	-2600	539	450
G (Bottom)	-10571	-9230	-9400		
H (Top)	-1700	-1630	-2035	403	278
H (Bottom)	-8920	-8980	-9120		
I (Top)	-1630	-1540	-2500	407	439
I (Bottom)	-9490	-8787	-7005		
J (Top)	-2463	-1079	-2075	480	347
J (Bottom)	-8610	-9140	-8900		

4.2.   Well Log Information

Fourteen well logs were imported from SONRIS and used in this study. These were supplemented with 45 logs made from driller notes found in the Department of Natural Resources files. Wells with elevations/information/data logged above 1000 ft of subsea depth were used (Figure 18). Formation tops were picked starting at the shallowest interpretable elevation to ensure consistency across the study area. Correlations were made on the tops of recognizable sands and shale marker patterns. Note, the sand and shale spontaneous potential log is reversed in these shallow well logs due to the formation fluid being freshwater in this zone (Figure 18). The 200 ft sand was picked in 9 wells within the study area. 5 gamma ray logs outside of the field area were used to confirm the 200 ft sand correlation. The 200 ft sand represents approximately the top of the Chicot Aquifer and is composed of varying amount of sand with multiple grain sizes. Its average elevation is -200 ft and a large quantity of clay overlies the sand. The "Water Works District #9" well was used for the initial correlations (Section 24, see location on Figure 17, 19, 20). This log begins at 0 ft and continues to a depth of -767 ft. In township 14 south, range 6 west, sections 14, 11, and 12, 4 wells log the shallow interval downthrown to Fault A. Fault B has one well log logged upthrown to it in section 7 and two wells logged downthrown that are also upthrown to Fault C (Figure 20). Fault D has one well with a shallow log downthrown in section 15. Fault E has one well with a shallow log immediately upthrown in section 18 and two wells are downthrown to it in section 24 and 20.
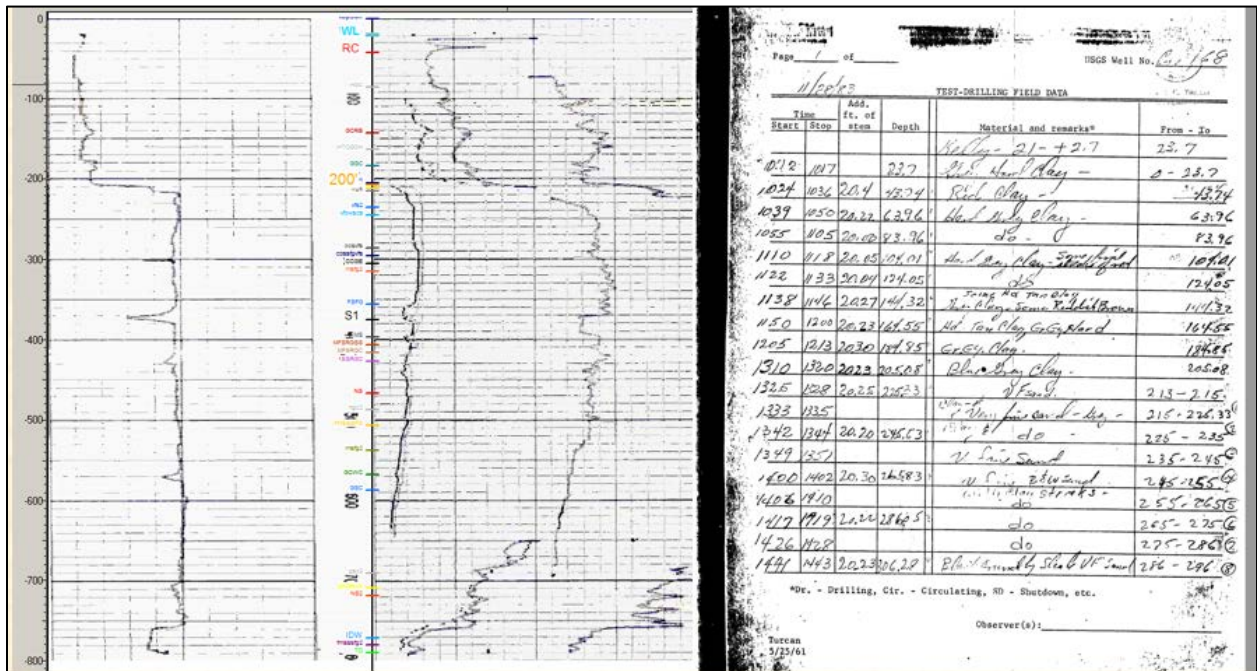
Figure 18: Water Works Well #9. Electric log with driller's notes assigned tops (Left). View of notes from 0 to ~300 feet (right).
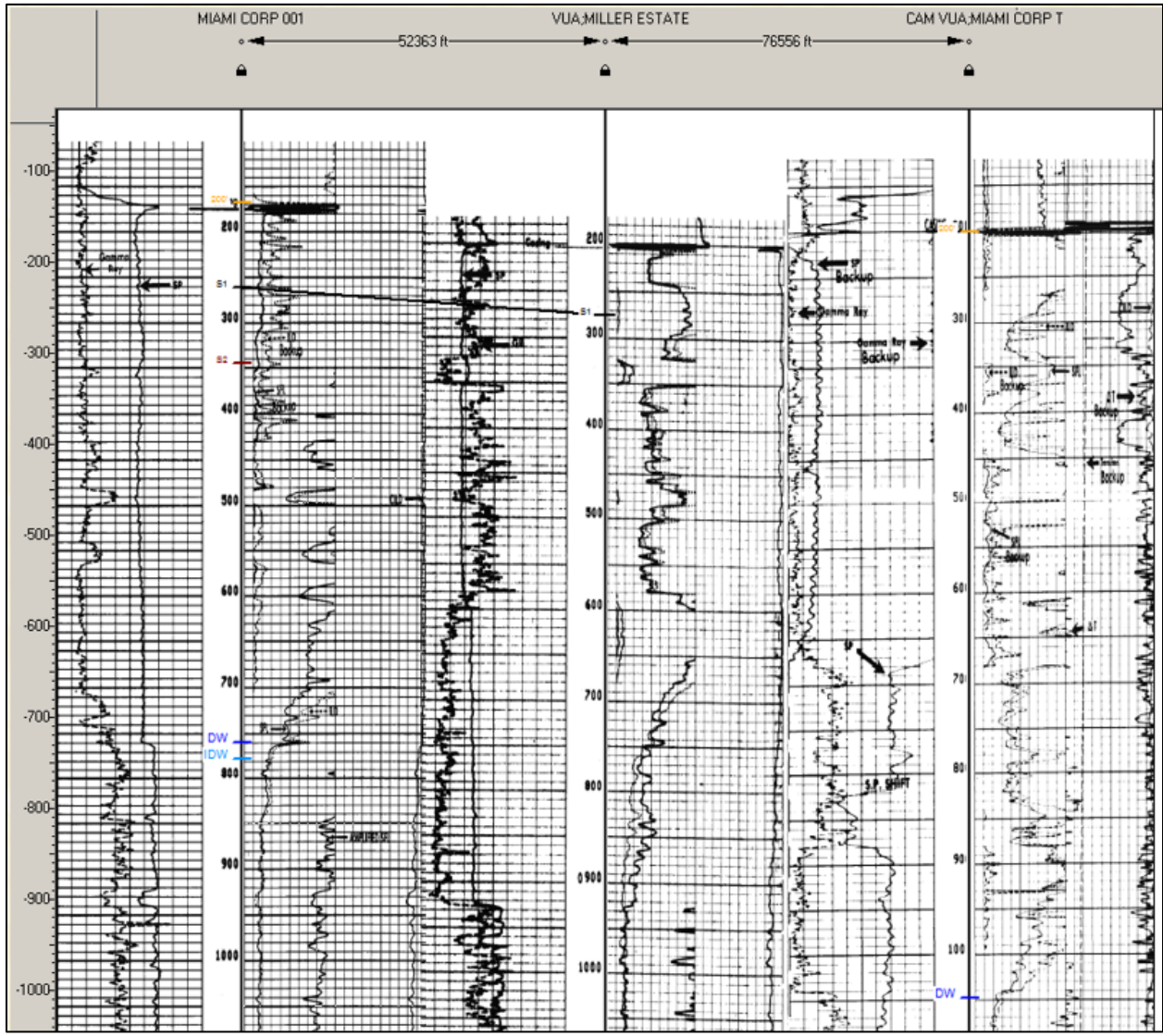
Figure 19: Gamma Ray vs SP - note gamma ray shows true lithology response while SP shows inverse

Descriptions from driller notes were brought into excel and assigned a color and or pattern. These were printed, scanned, depth registered, and correlated in Kingdom. A total of 45 monitor well driller logs were used with 32 unique descriptions denoting the lithology of the upper 300 ft. Typically, the lithology fell in to two categories: sand or shale/clay. The top and base of shale along with the top of sand were correlated across this area. These formation tops were used to generate an isochore while the top of sand formations aided in delineating the general structures in the study area.

The top of sand was shallowest in sections 11 and 12 within the graben, downthrown to all faults. The isochore of clay is thinnest in this area and thickens towards the faults. The average top of sand, and therefore, base of clay, is -151 ft. The average thickness of clay is 168 ft. The average thickness of clay downthrown within the graben is 116 ft. The average static water level is -19 feet.
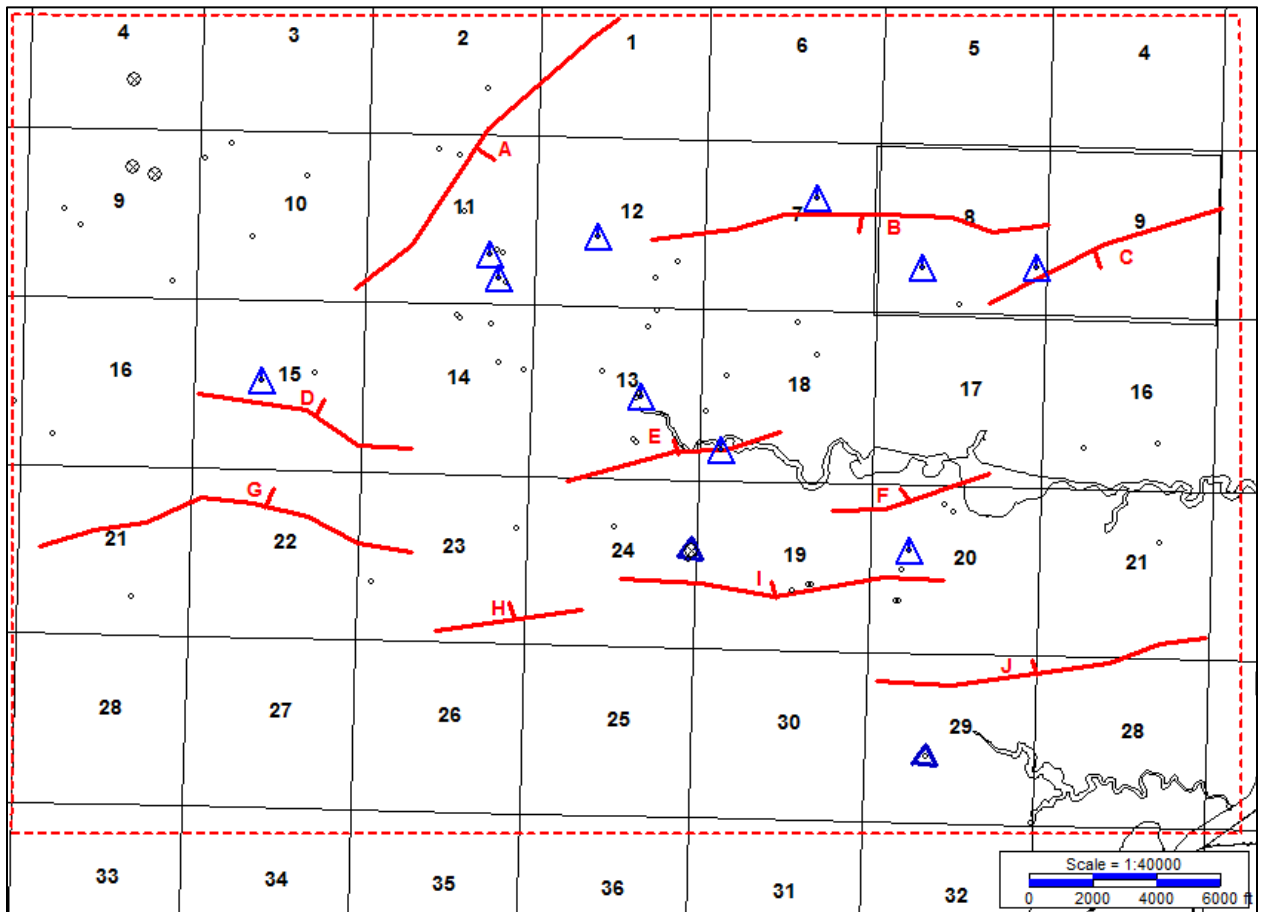
Figure 20: Location of electric logs (blue triangles) and rig supply water wells (grey dots). Adapted from Kingdom.

4.3. Expansion Index

Four horizons, H1, H2, H3, and H4 were picked using the seismic dataset on the central section of Faults A through J on both their upthrown and downthrown sides of the fault (Figure 21). The depths between each pair of horizon were noted as their interval thicknesses. These thicknesses were used to compare the ratio of thicknesses between the upthrown and downthrown sides of the fault. For example, subtracting the depth of H1 from H2 would yield the thickness for both upthrown and downthrown. The thickness of the downthrown side is divided by the thickness of the upthrown side in which the quotient defined as the expansion index (E) (Table 3). An expansion index greater than one or less than one implies stratigraphic thickening or thinning of the units in the hanging wall, respectively (Figure 22).

$$Expansion\ I = \frac{(Downthrown\ H2\ depth - Downthrown\ H1\ depth)}{(Upthrown\ H2\ depth - Upthrown\ H1\ depth)}$$

Table 3: Expansion index

Fault	Expansion index		
	E1	E2	E3
A	1.23	0.84	1.03
B	1.00	1.03	1.04
C	1.13	0.98	0.89
D	1.04	1.03	1.05
E	1.03	1.04	0.99
F	1.08	1.06	1.01
G	1.06	1.06	1.11
H	1.31	0.83	1.10
I	0.88	1.10	1.13
J	1.05	1.05	1.00
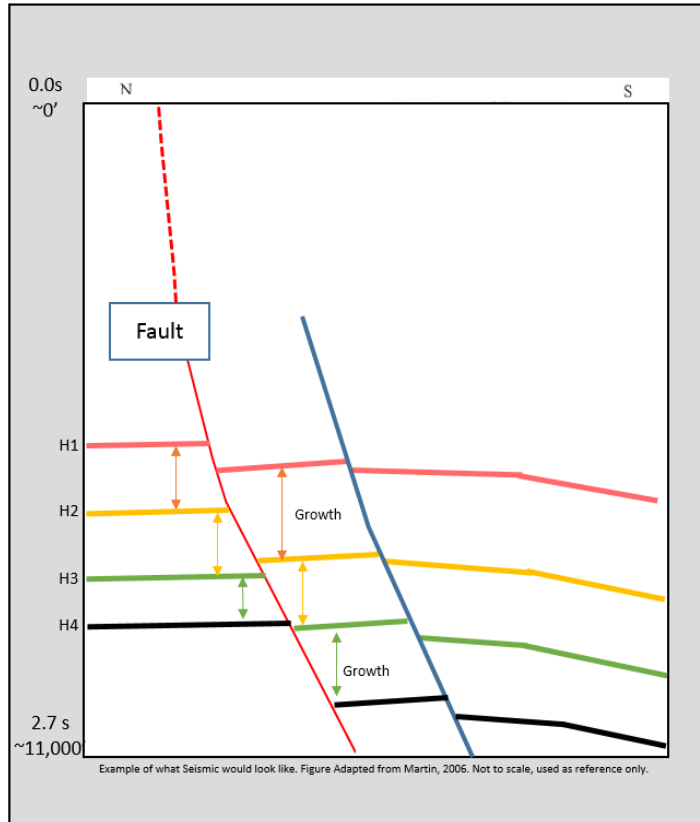
Figure 21: Idealized cross section of expansion index. Growth observed between H1 and H2 and H3 and H4
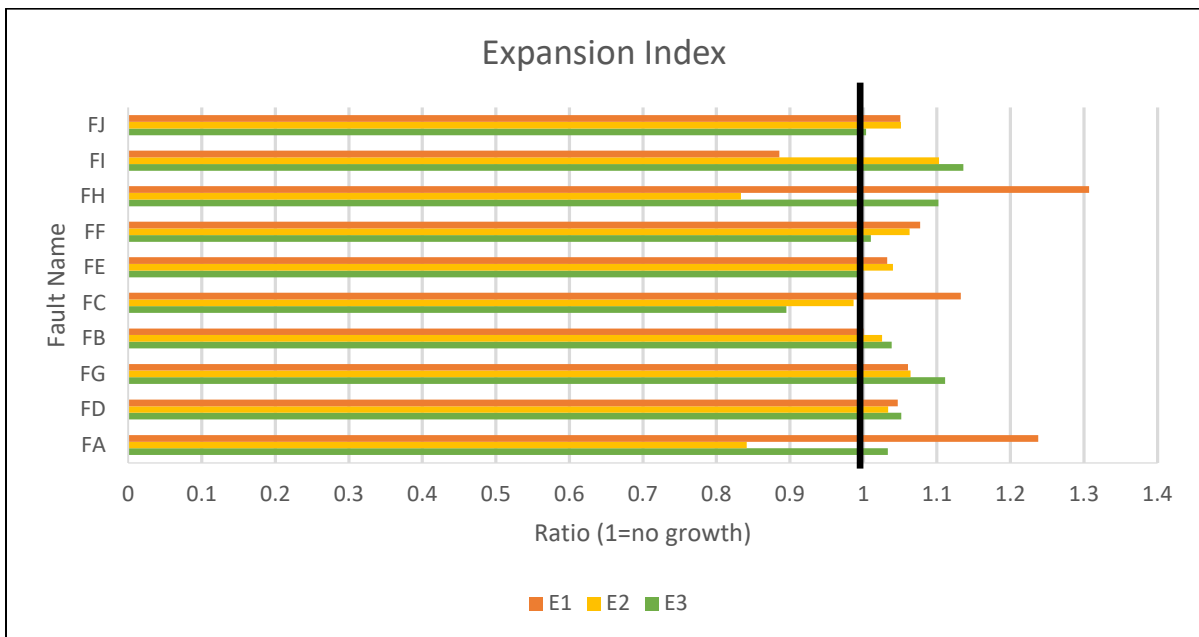
Figure 22: Expansion index. Bars past 1 indicate growth. E1 is the shallowest expansion. FA indicates Fault A, etc.

4.4.   Fault Surface Characteristics

Within the study area, detailed analysis of the seismic survey revealed the presence of 10 fault surfaces that were suspected to travel to the surface (Figure 23.). Faults were projected to the surface, maintaining constant dip of the fault surface. Elevation transects were conducted perpendicular to the strike of the projected fault surface trace (Figure 26). The transect elevations were averaged for comparison to the average elevation of the upthrown and downthrown (Tables 5-14). Three of these faults were located in the north of the study area and dip down to south (A-C), while all the other faults dip to the north (D-J), forming an east-west oriented graben (Figure 14, 16, 17, 23). For consistency, the mean elevation of the upthrown and downthrown sides of faults were taken over an area of approximately equal size, by drawing polygons using connecting points from the transects and surface fault projection ends (Figure 24). The LIDAR's elevation points were averaged within upthrown and downthrown area of the faults and indicates the mean elevation of the area on either side of the surface fault projections (Figure 25, Table 5-14). The vertical accuracy of the points is 6 to 12 inches. 12 inches (1 foot) was used as the error for the elevation transects.

Table 4: Fault characteristics at the surface

Fault	Length (miles)	Sections	Strike	Dip
A	2.25	11, 2, 1	NE-SW	S-SE
B	2.40	12, 7, 8	E-W	S
C	1.50	8, 9	NE-SW	S-SE
D	1.40	15, 14	E-W	N
E	1.35	13, 18	E-W	N
F	1.00	19, 20, 17	E-W	N
G	2.27	21, 22, 23	E-W	N
H	0.88	23, 24	E-W	N
I	1.95	24, 19, 20	E-W	N
J	1.87	29, 28, 21	E-W	N
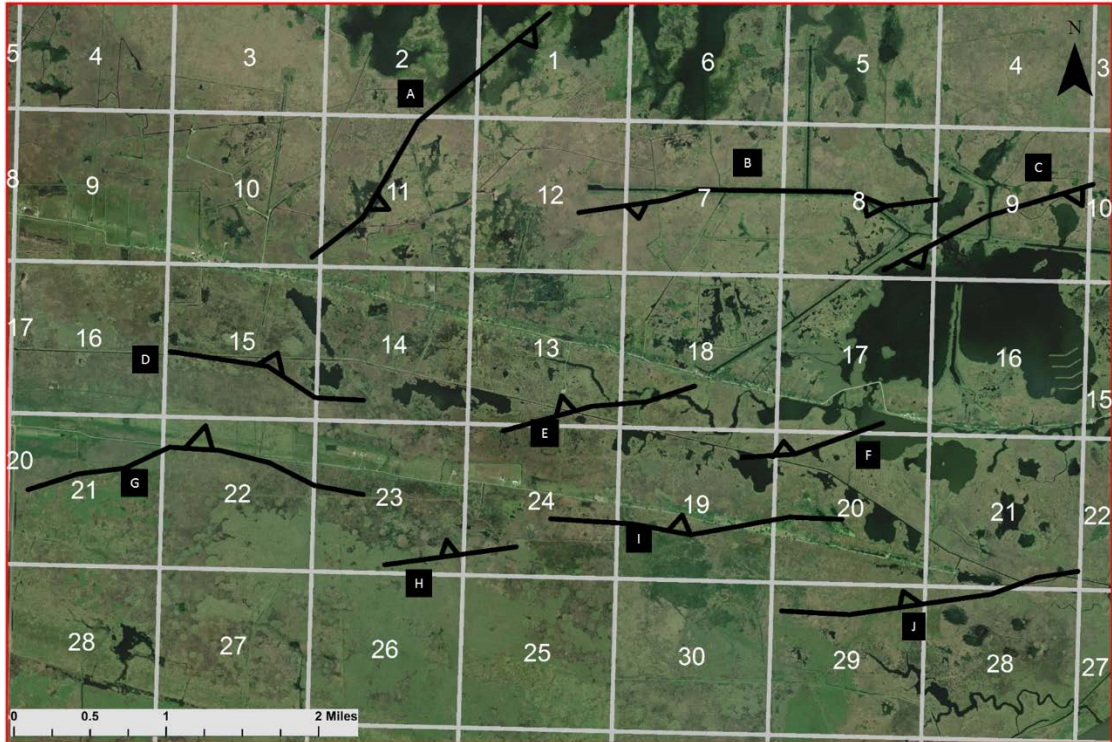
Figure 23: Field area with sections and fault surface traces
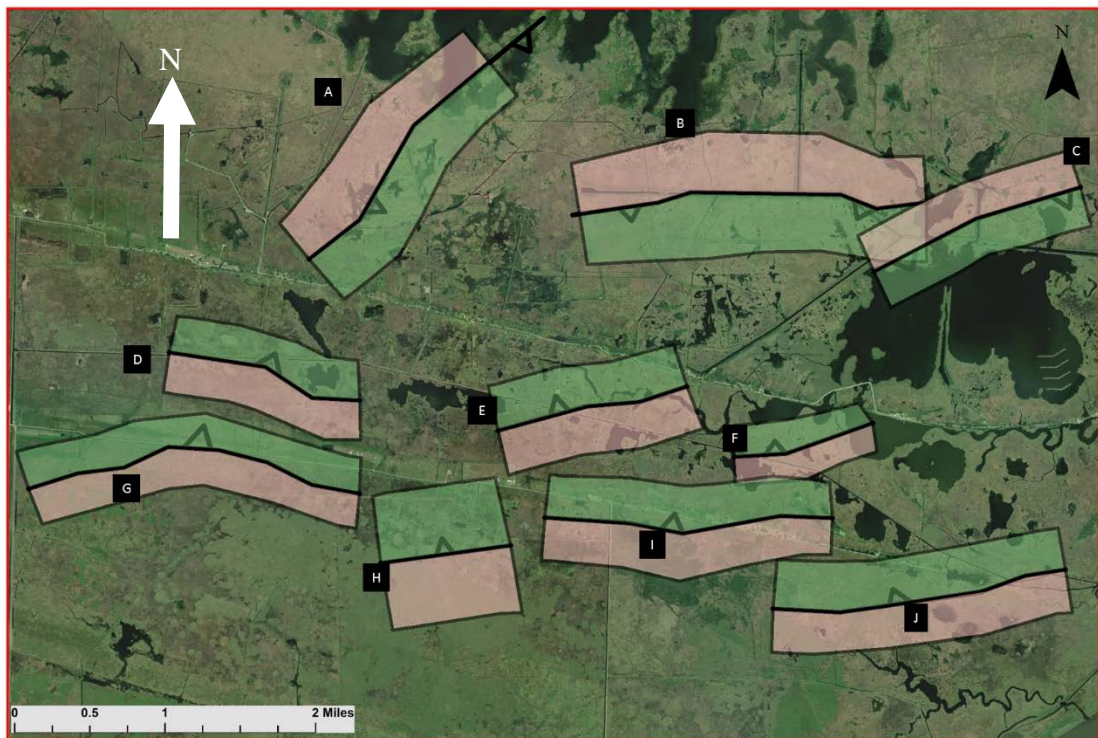
Figure 24: Upthrown (red) and downthrown (green) areas comparison
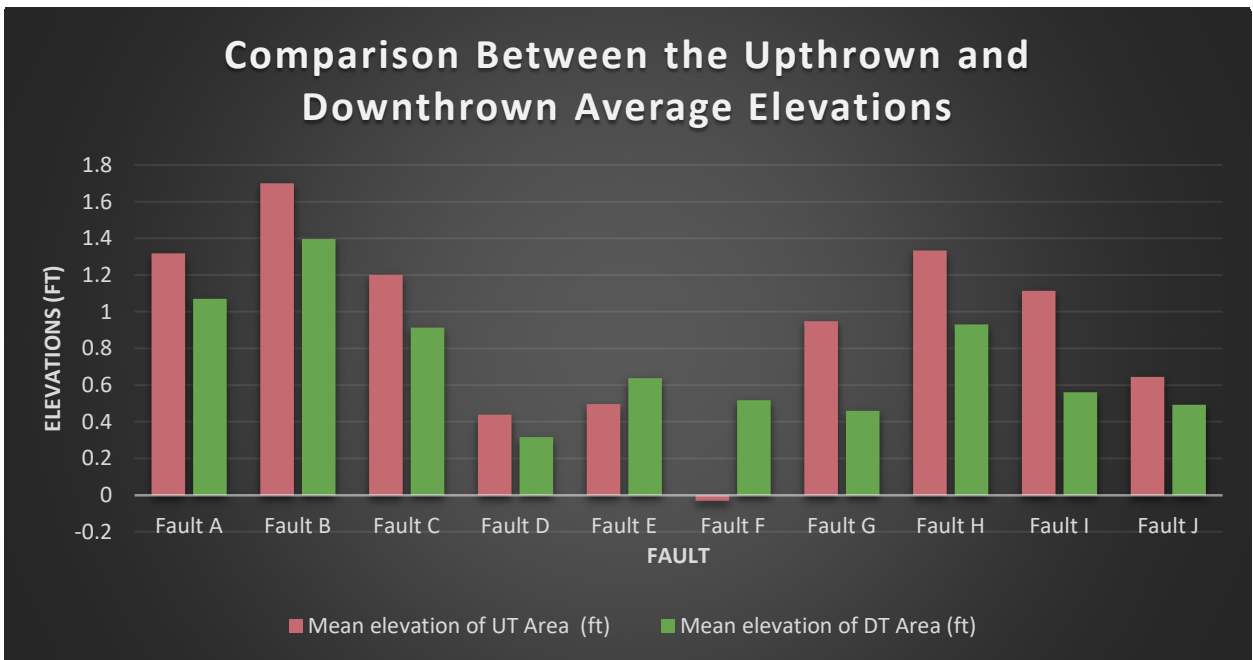
Figure 25: Comparison between average elevations and the areas measured UT is upthrown and DT is downthrown)
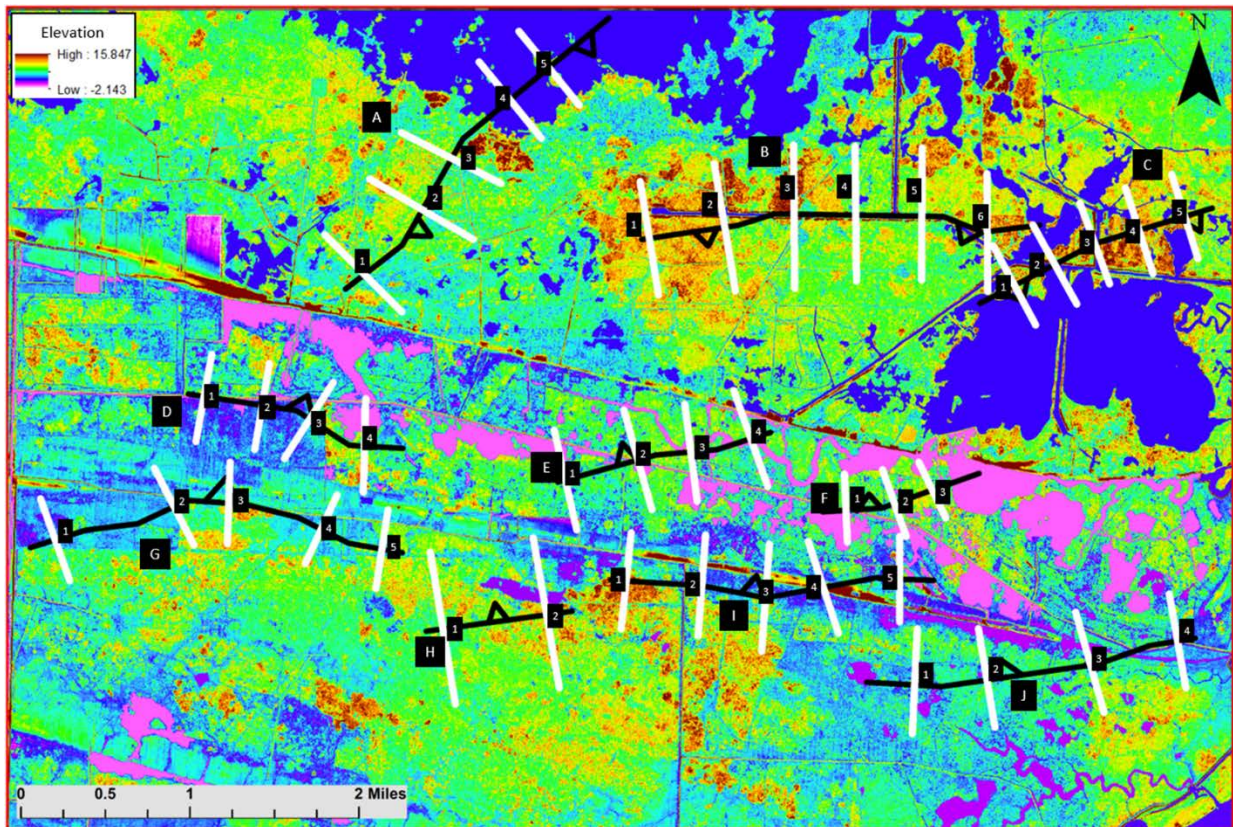
Figure 26: LIDAR with fault surfaces and transects

4.4.1. Fault A. Fault A's average upthrown elevation is 0.96 ft and downthrown its 0.94 ft. When the elevations from open water on the northeast end of the fault are removed out, the average elevation upthrown is 1.32 ft and downthrown it is 1.07 ft and are the numbers reflected in figure 25.

Table 5: Fault A surface data.

Transect #	Length (ft)	Average Upthrown Elevation (± 1 ft)	Average Downthrown Elevation (± 1 ft)
FA1	3660	1.46	0.50
FA2	3540	1.78	0.85
FA3	2880	1.37	0.97
FA4	3060	0.12	0.54
FA5	2940	0.27	0.86
Average Transect Elevation		1.00	0.74
Average Area Elevation		0.96	0.94
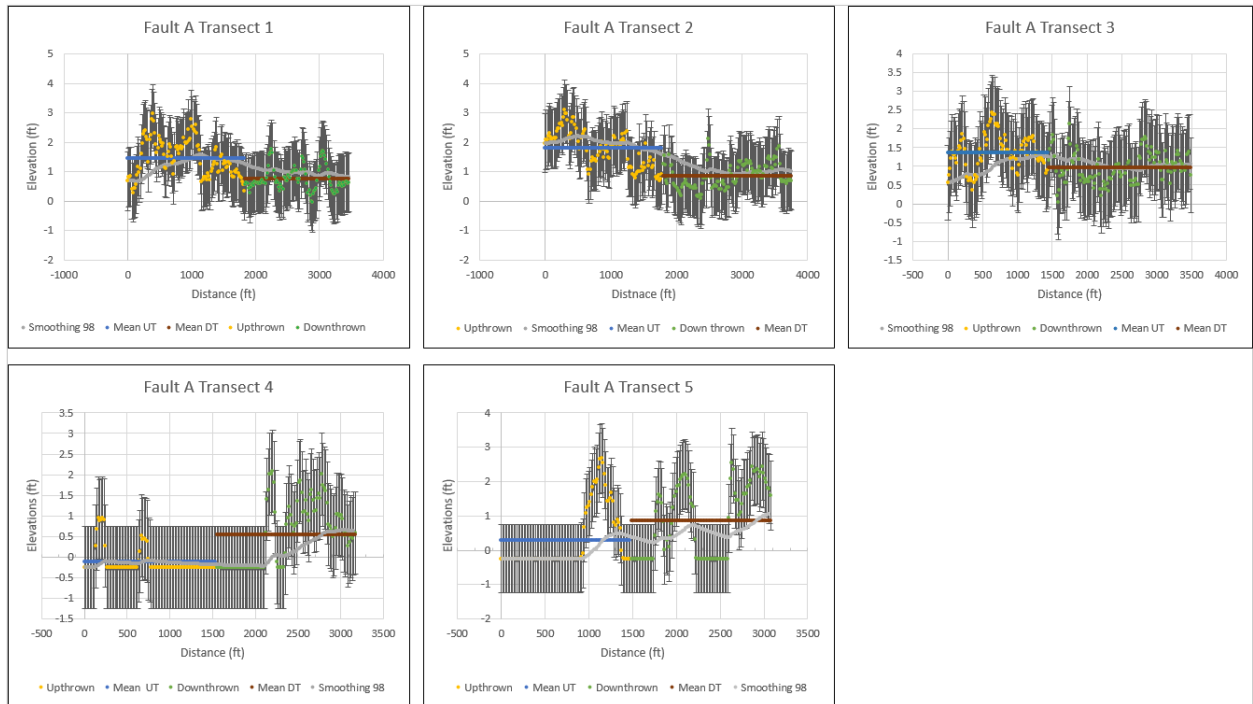
Figure 27: Elevation profile across Fault A obtained from LIDAR data. Upthrown (yellow), downthrown (green), mean upthrown (blue), mean downthrown (brown), and smoothing average of elevation (grey)

4.4.2. Fault B. Fault B's average upthrown elevation is 1.70 ft and downthrown it is 1.40 ft.

Table 6: Fault B surface characteristics.

Transect #	Length (ft)	Average Upthrown Elevation (± 1 ft)	Average Downthrown Elevation (± 1 ft)
FB1	3540	2.11	1.50
FB2	3930	1.79	1.92
FB3	4320	2.63	1.23
FB4	4270	1.13	1.47
FB5	4100	1.99	1.38
FB6	3540	2.16	1.02
Average Transect Elevation		1.97	1.42
Average Area Elevation		1.70	1.40
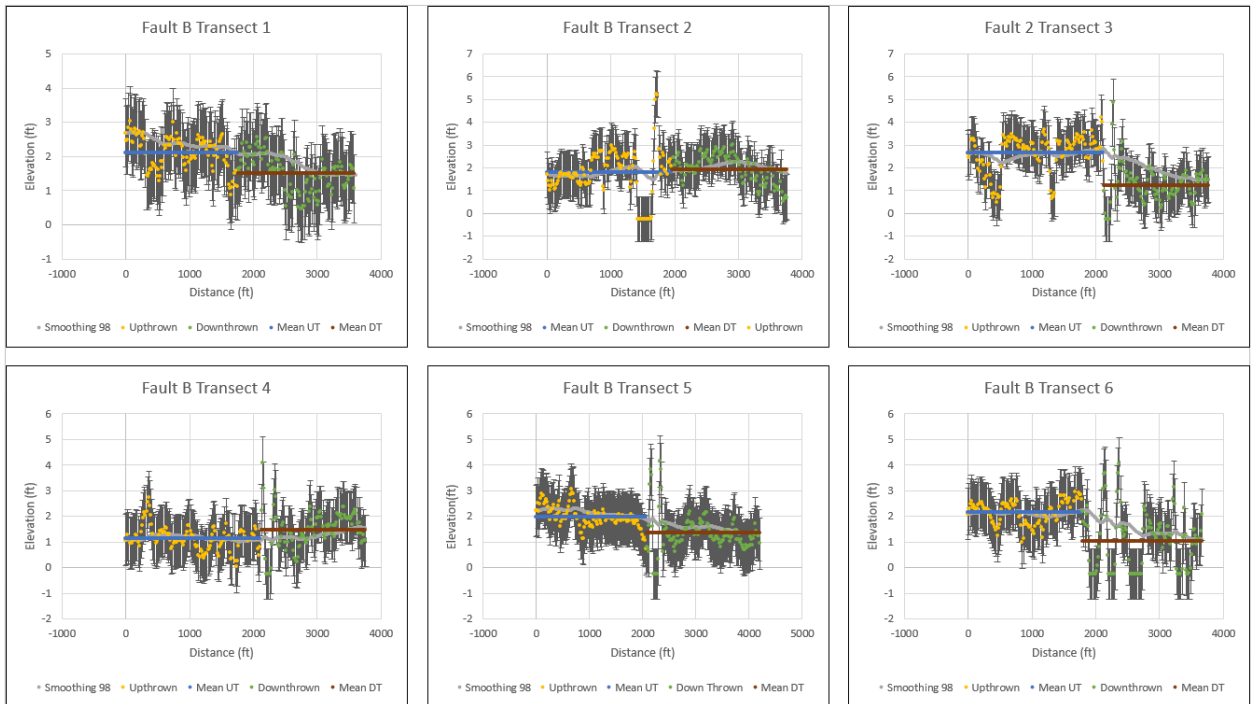
Figure 28: Elevation profile across Fault B obtained from LIDAR data. Upthrown (yellow), downthrown (green), mean upthrown (blue), mean downthrown (brown), and smoothing average of elevation (grey)

4.4.3. Fault C. Fault C's average upthrown elevation is 1.20 ft and downthrown it is

0.91 ft. The downthrown side of Fault C is exposed to openwater contributing to the lower

elevations, in particular Transects 1 and 2.

Table 7: Fault C surface characteristics.

Transect #	Length (ft)	Average Upthrown Elevation (± 1 ft)	Average Downthrown Elevation (± 1 ft)
FC1	2820	1.39	-0.02
FC2	2720	0.81	-0.03
FC3	2280	1.46	1.14
FC4	2460	1.68	2.01
FC5	2745	1.45	1.17
Average Transect Elevation		1.36	0.85
Average Area Elevation		1.20	0.91
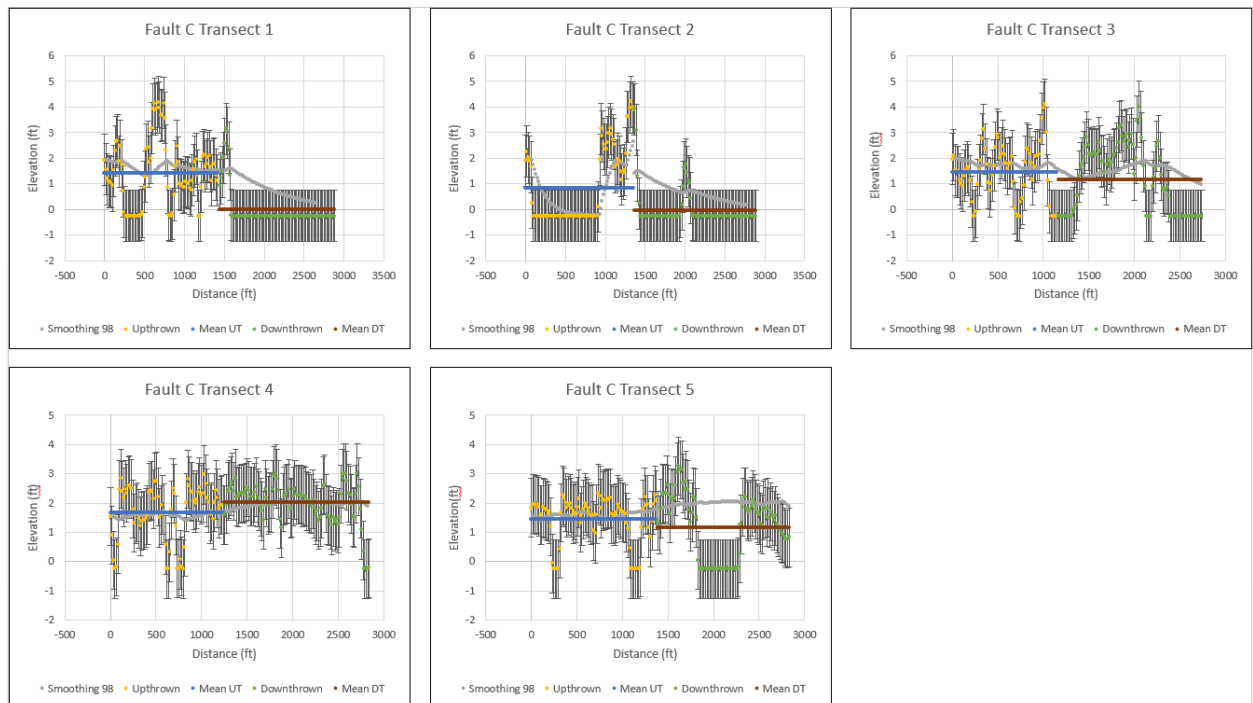
Figure 29: Elevation profile across Fault C obtained from LIDAR data. Upthrown (yellow), downthrown (green), mean upthrown (blue), mean downthrown (brown), and smoothing average of elevation (grey)

4.4.4. Fault D. Fault D's average upthrown elevation is 0.44 ft and downthrown it is 0.31 ft. Transect 4 crosses medium sized pond on the immediate downthrown side of the fault surface trace.

Table 8: Fault D surface characteristics.

| Transect #	Length (ft)	Average Upthrown Elevation (± 1 ft)	Average Downthrown Elevation (± 1 ft)
FD1	2800	0.11	0.47
FD2	2720	0.54	0.95
FD3	287	0.2	0.36
FD4	2920	1.59	-0.14
Average Transect Elevation		0.61	0.41
Average Area Elevation		0.44	0.31
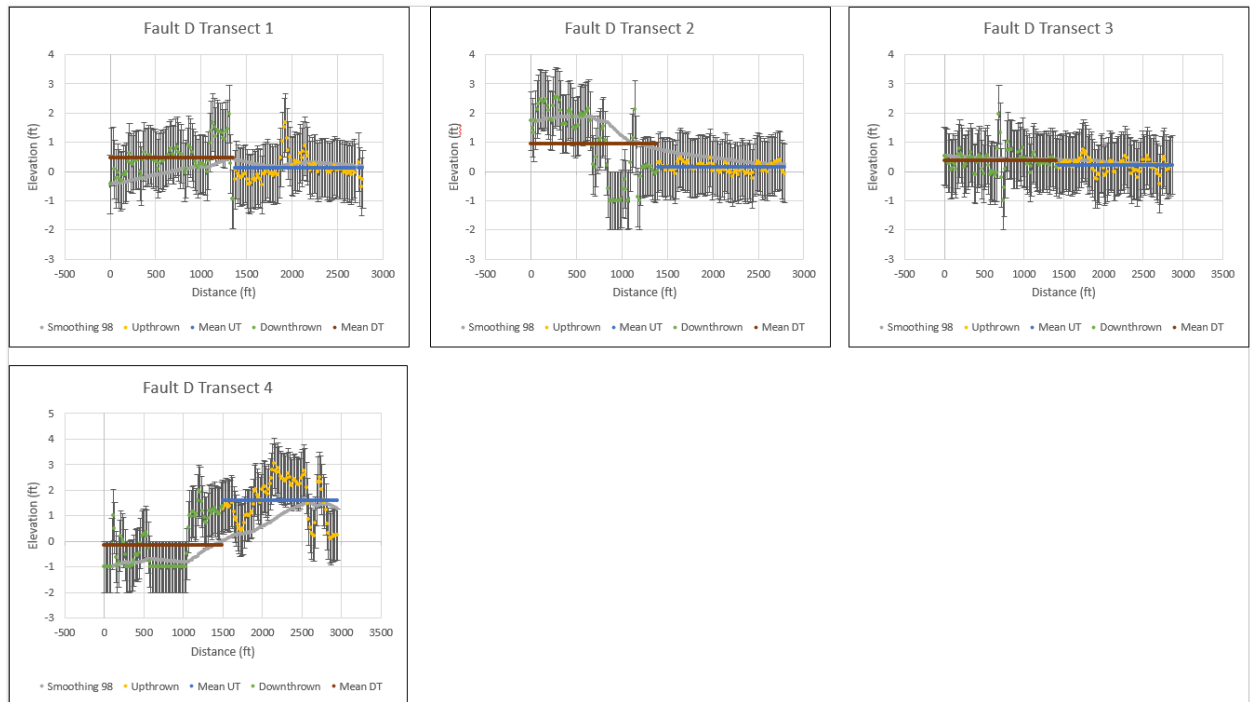
Figure 30: Elevation profile across Fault D obtained from LIDAR data. Upthrown (yellow), downthrown (green), mean upthrown (blue), mean downthrown (brown), and smoothing average of elevation (grey)

4.4.5. Fault E. Fault E is one of two faults that have a negative offset (downthrown is higher in elevation than upthrown). Several smaller ponds are found in the upthrown side contributing low elevations reducing the average of the upthrown. Downthrown, a river/stream follows the strike of the fault.

Table 9: Fault E surface characteristics.

| Transect #	Length (ft)	Average Upthrown Elevation (± 1 ft)	Average Downthrown Elevation (± 1 ft)
FE1	3180	0.43	0.07
FE2	322	0.80	0.38
FE3	3050	-0.05	0.75
FE4	3170	0.21	0.56
Average Transect Elevation		0.35	0.44
Average Area Elevation		0.50	0.64
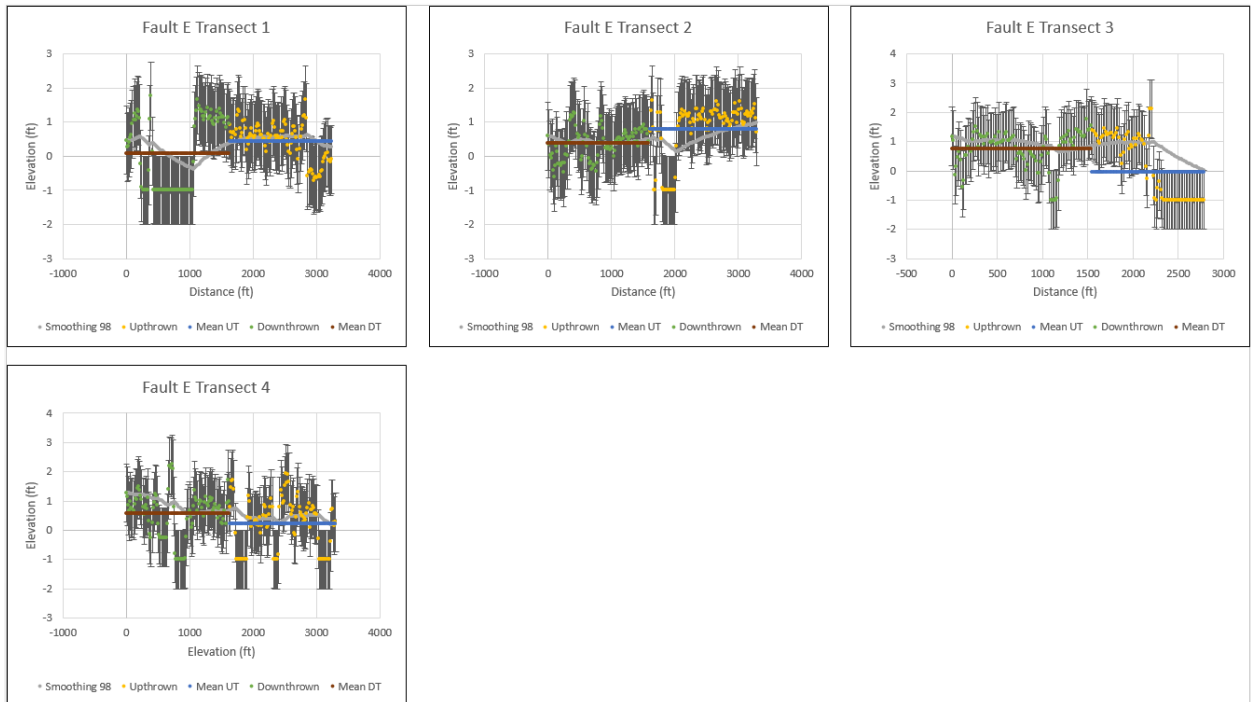
Figure 31: Elevation profile across Fault E obtained from LIDAR data. Upthrown (yellow), downthrown (green), mean upthrown (blue), mean downthrown (brown), and smoothing average of elevation (grey)

4.4.6. Fault F. The second fault that has a negative offset. Fault F's transect 1 and 2 upthrown side is over a majority of water. A medium pond on the west end contributes to the lower elevations on the upthrown side.

Table 10: Fault F surface characteristics.

| Transect #	Length (ft)	Average Upthrown Elevation (± 1 ft)	Average Downthrown Elevation (± 1 ft)
FF1	2120	-0.89	0.91
FF2	2210	0.90	0.39
FF3	1930	0.61	0.68
Average Transect Elevation		0.21	0.66
Average Area Elevation		-0.03	0.52
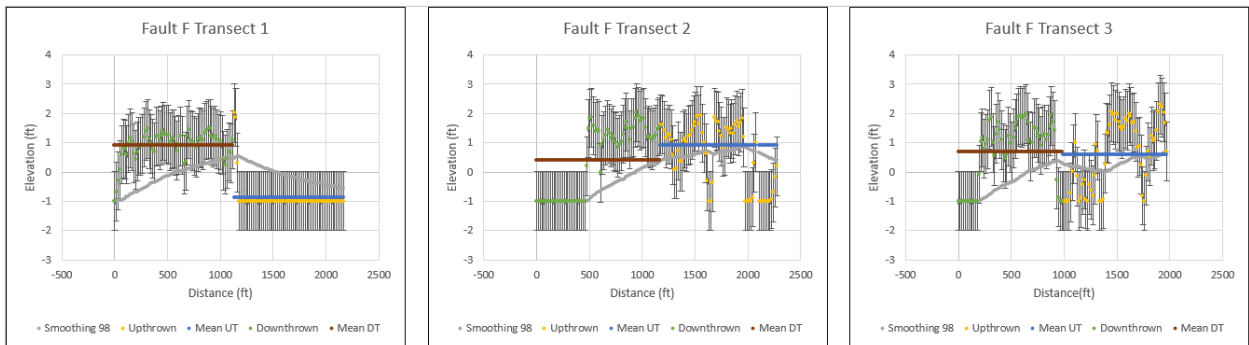
Figure 32: Elevation profile across Fault F obtained from LIDAR data. Upthrown (yellow), downthrown (green), mean upthrown (blue), mean downthrown (brown), and smoothing average of elevation (grey)

4.4.7. Fault G. Fault G has a positive offset of 0.49 ft, Chenier Perdue is on the downthrown side.

Table 11: Fault G surface characteristics.

| Transect #	Length (ft)	Average Upthrown Elevation (± 1 ft)	Average Downthrown Elevation (± 1 ft)
FG1	2710	0.99	0.14
FG2	2700	1.12	0.39
FG3	2540	1.38	0.41
FG4	2350	1.02	0.58
FG5	2480	1.55	0.78
Average Transect Elevation		1.21	0.46
Average Area Elevation		0.95	0.46
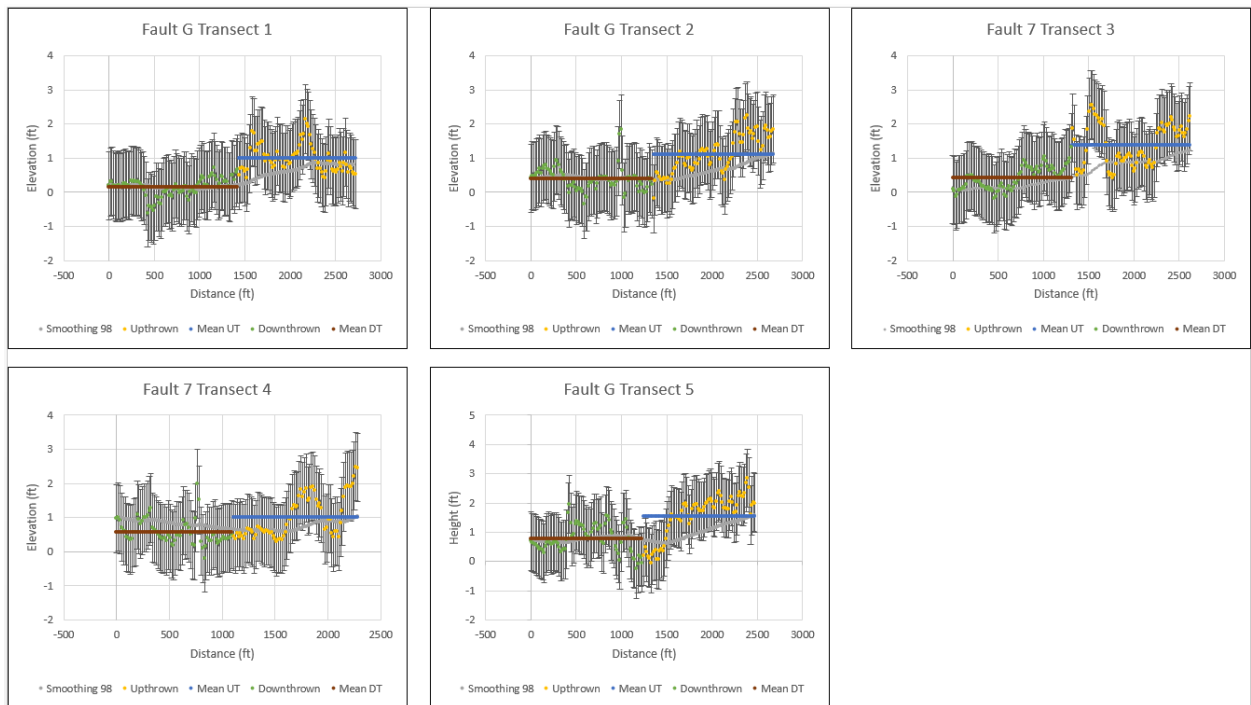
Figure 33: Elevation profile across Fault G obtained from LIDAR data. Upthrown (yellow), downthrown (green), mean upthrown (blue), mean downthrown (brown), and smoothing average of elevation (grey)

4.4.8. Fault H. Fault H shows how transects can vary dramatically across the fault. Transect 1 has a negative offset of 0.28 ft while Transect 2 has a positive offset of 0.84 ft. The average of the upthrown area is 1.33 ft and downthrown it is 0.93 ft.

Table 12: Fault H surface characteristics.

| Transect #	Length (ft)	Average Upthrown Elevation (± 1 ft)	Average Downthrown Elevation (± 1 ft)
FH1	4860	0.98	1.26
FH2	4760	1.41	0.57
Average Transect Elevation		1.19	0.92
Average Area Elevation		1.33	0.93
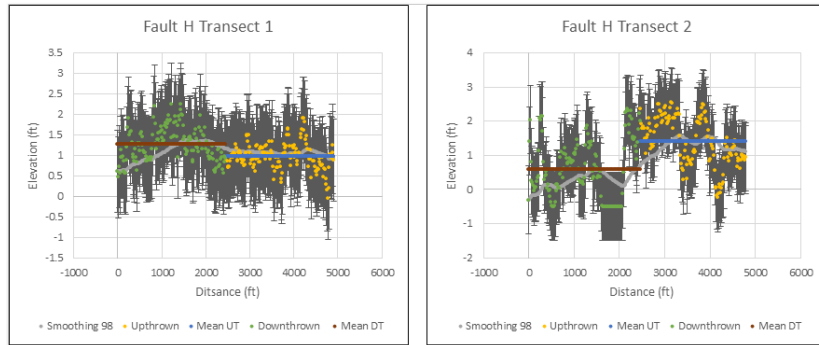
Figure 34: Elevation profile across Fault H obtained from LIDAR data. Upthrown (yellow), downthrown (green), mean upthrown (blue), mean downthrown (brown), and smoothing average of elevation (grey)

4.4.9. Fault I. Fault I's average area elevation is 0.56 ft in positive offset between the upthrown and downthrown.

Table 13: Fault I surface characteristics.

| Transect #	Length (ft)	Average Upthrown Elevation (± 1 ft)	Average Downthrown Elevation (± 1 ft)
FI1	3010	2.15	0.45
FI2	3160	2.24	0.81
FI3	3350	1.6	0.47
FI4	3020	0.65	0.59
FI5	2670	0.71	0.31
Average Transect Elevation		1.47	0.53
Average Area Elevation		1.12	0.56
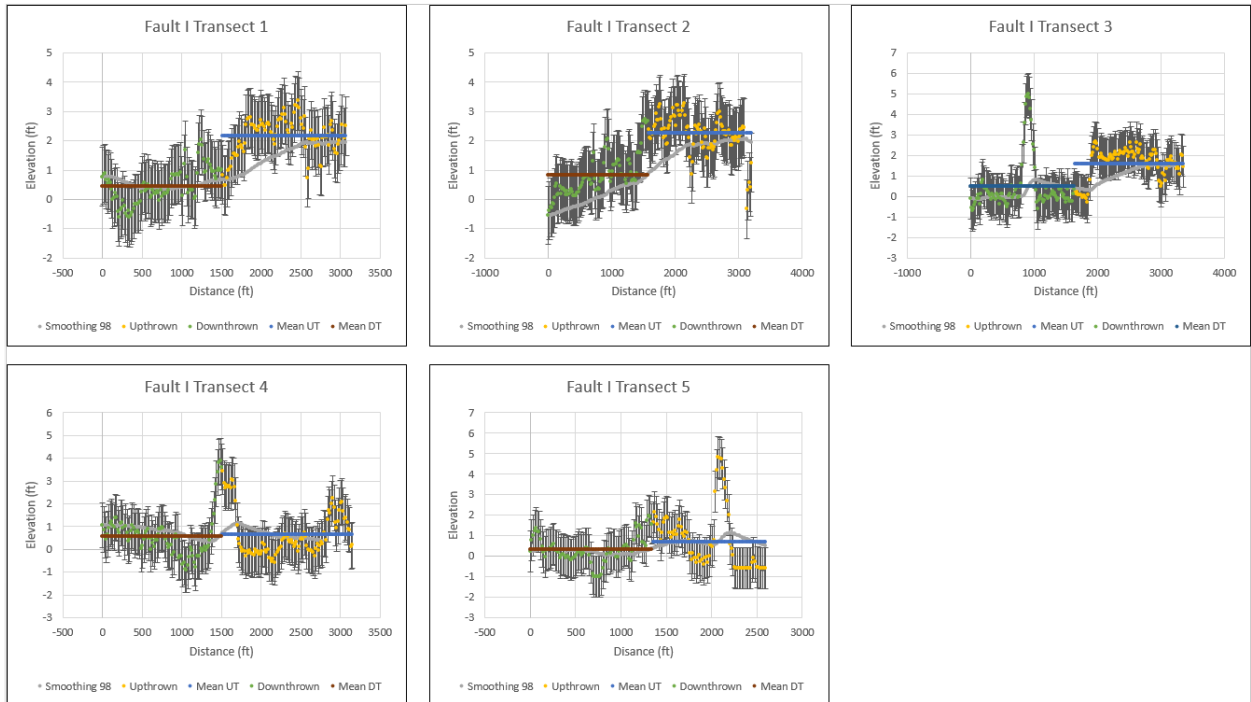
Figure 35: Elevation profile across Fault I obtained from LIDAR data. Upthrown (yellow), downthrown (green), mean upthrown (blue), mean downthrown (brown), and smoothing average of elevation (grey)

4.4.10. Fault J. Fault J has a positive offset of 0.16 ft between the upthrown and downthrown elevations.

Table 14: Fault J surface characteristics.

| Transect #	Length (ft)	Average Upthrown Elevation (± 1 ft)	Average Downthrown Elevation (± 1 ft)
FJ1	3270	0.46	0.89
FJ2	3120	0.55	0.50
FJ3	3250	1.29	0.39
FJ4	2980	0.47	0.32
Average Transect Elevation		0.69	0.53
Average Area Elevation		0.65	0.49
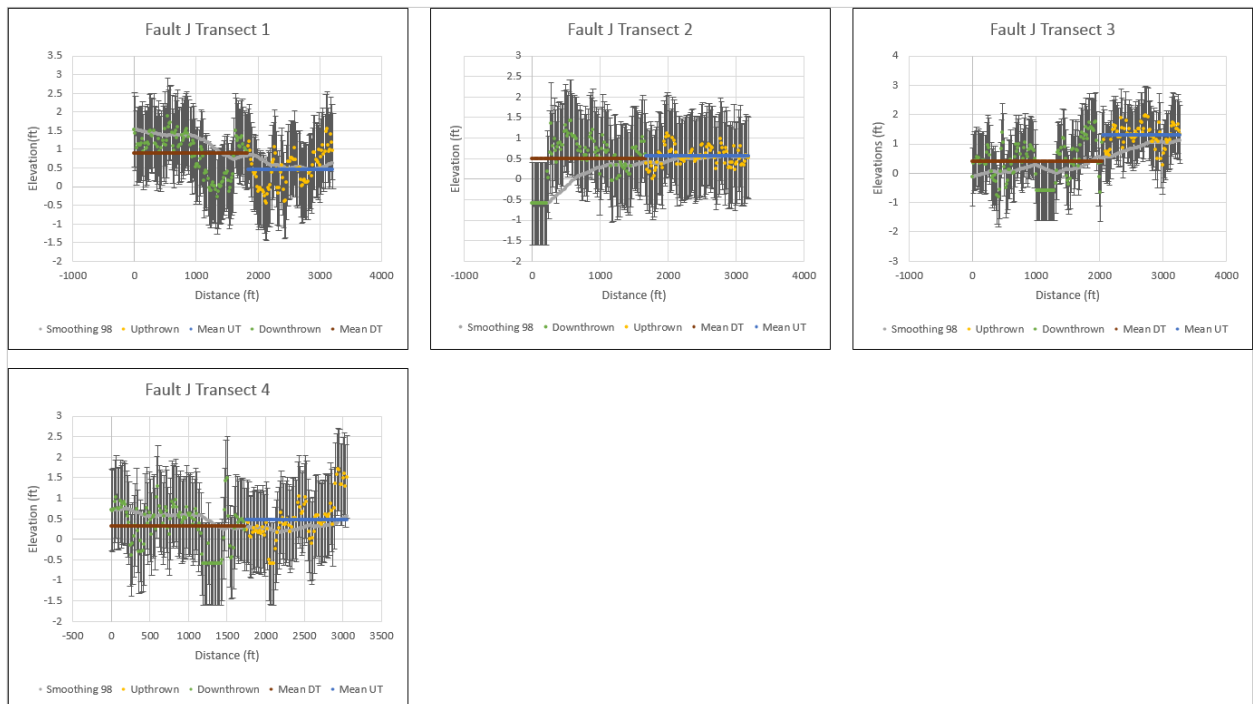
Figure 36: Elevation profile across Fault J obtained from LIDAR data. Upthrown (yellow), downthrown (green), mean upthrown (blue), mean downthrown (brown), and smoothing average of elevation (grey)

4.5. Aerial Photos

A total of 21 aerial photographs were stitched together in ArcMap (Figure 37). These images show the landscape of the study area landscape in 1953 at a 1:20000 scale. These images were compared to aerial photographs and satellite images taken in 2017(Figures 38 & 39).
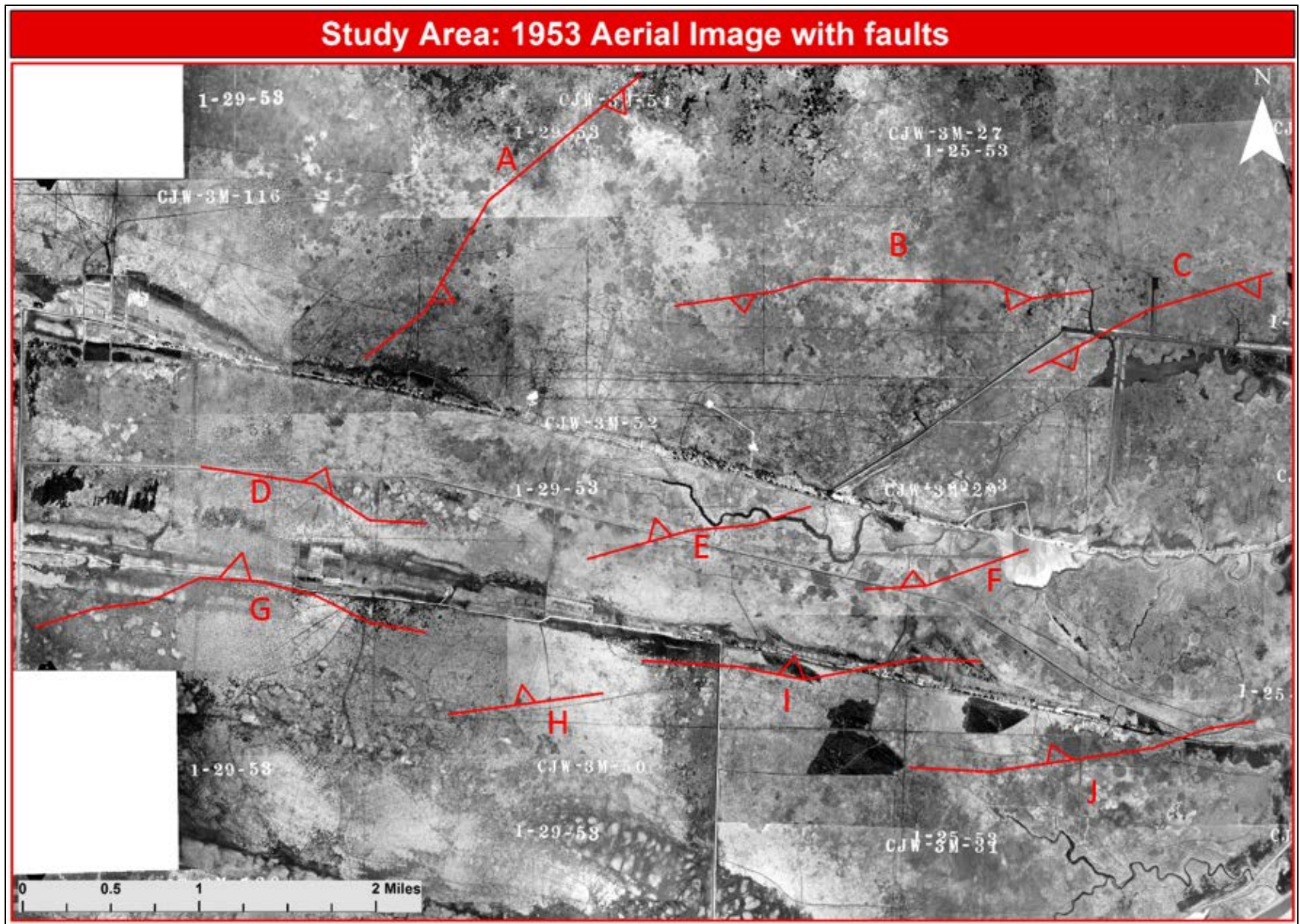
Figure 37: Mosaic aerial photograph from LSU Cartographic research center
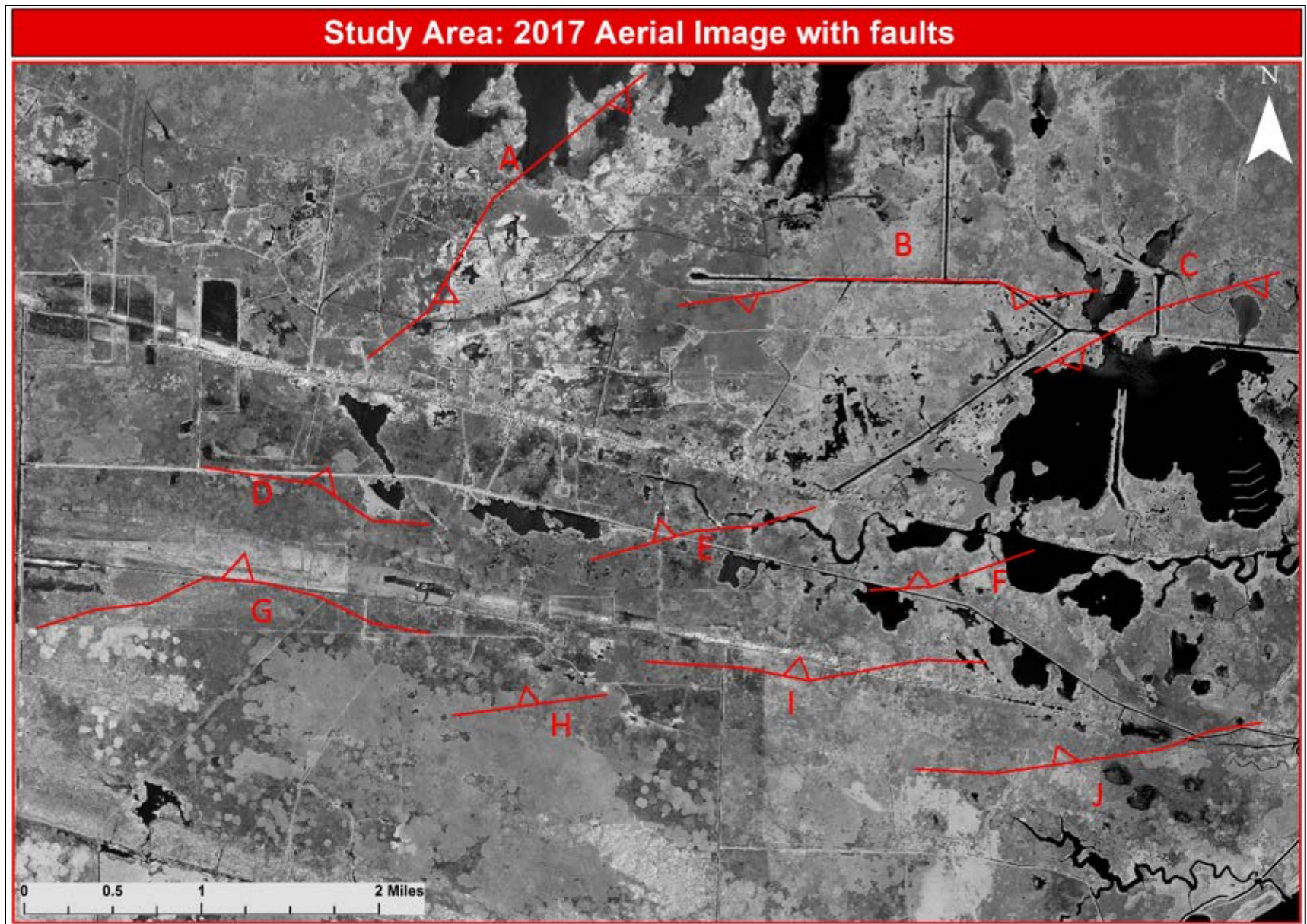
Figure 38: Aerial photograph adapted from earth explorer
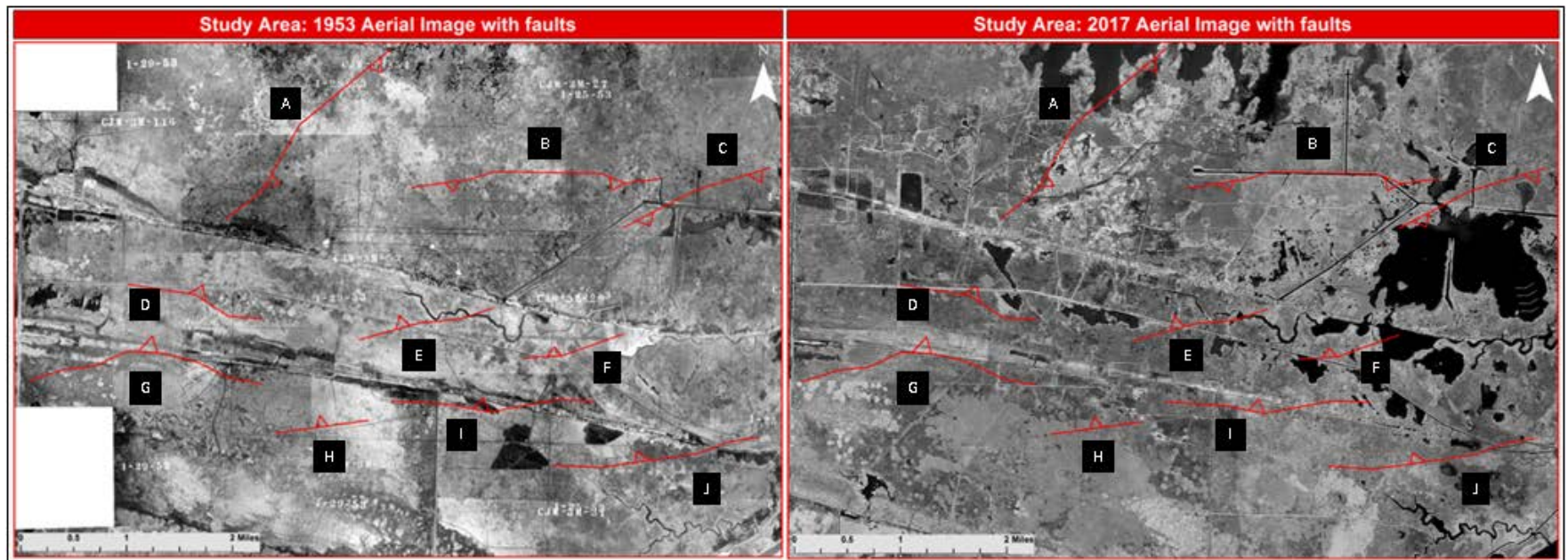
Figure 39: Aerial image from 1953 juxtaposed to one from 2017.

4.5.1. Fault A. Fault A takes up two frames, 2M-54 and 2M-56 and end is bounded by cheniers on its southern end (Figure 40). Much of the land is scarred by what might be trapper routes and canals. Open water is present in the northeast end of the fault. The vegetation present resembles Spartina Patins and Rozo Cane (Fragmitis, the clump circles). The southwest end of the fault ends on the north side of Little Chenier. The modern day image shows that the northeast area has much higher degree of open water on the upthrown and downthrown sides of where the fault runs. In the southwest area, the suspected surface fault runs directly through open water. Approximately 3000 feet to the southeast, downthrown to the fault, the land is dominated by manmade pools of water.

Figure 40: Aerial photograph highlighting Fault A in 1953 (left) and 2017 (right).

4.5.2. Fault B. Fault B occupies frames 2M-27 and 2M-165 (Figure 41). In the 1953 images, heavily scarred land is present on both the upthrown and downthrown sides. More Rozo Cane is found on the southern side of the fault. In the 1953 image, two treaded tracks south of the central portion of the fault run east west, suggesting the marsh is strong enough to support vehicles. The modern day image shows ponds on the downthrown side of the fault. A canal runs directly along the strike of the fault. There is a more water on the eastern side of the fault.

Figure 41: Aerial photograph highlighting Fault B in 1953 (left) and 2017 (right).

4.5.3. Fault C. Fault C occupies one frame, 2M-165, in the 1953 aerial photographs (Figure 42). There is significantly more land present in the 1953 image. The land is scarred on the upthrown side. To the south, downthrown of the fault, a canal runs east-west. In addition, there is a small bayou/stream/river offshoot south of the Mermentau River. It runs to the southwest in a smooth arcuate trajectory till it meets another stream running east west from the Mermentau River. The modern day image shows an immediate difference from the photographs of 1953: a large lake has formed immediately downthrown to Fault C to the south, within the bounds of the stream present in 1953. This drainage pattern is sub parallel to the surface fault. To the south of Fault C, a canal runs north south with levees on either side of it. These levees may contribute to preventing sheet flow across the pond.
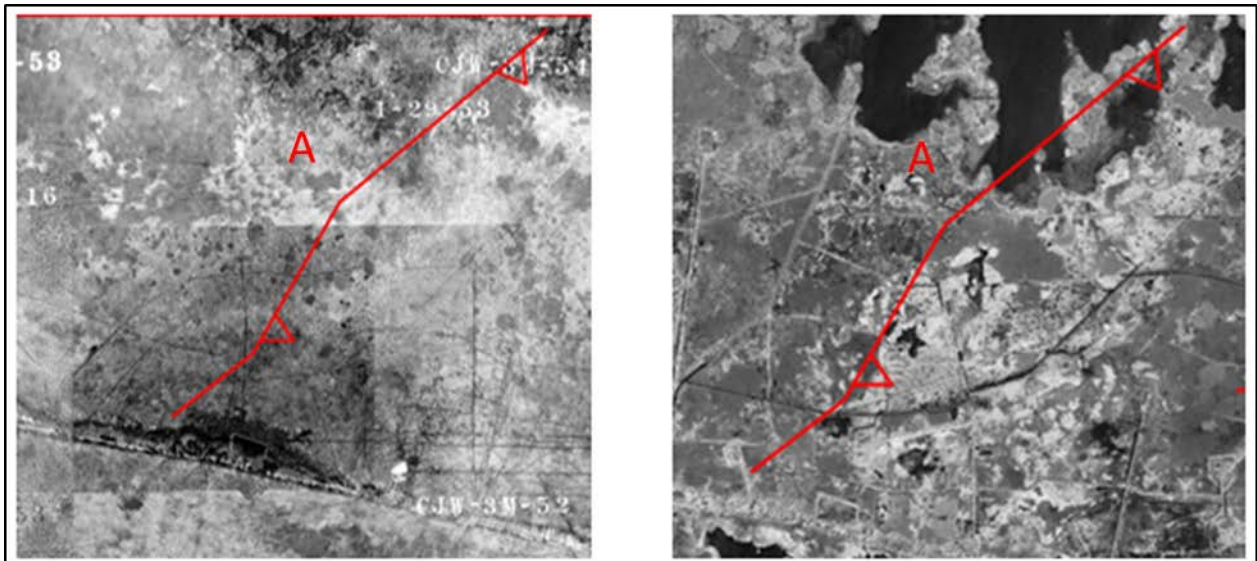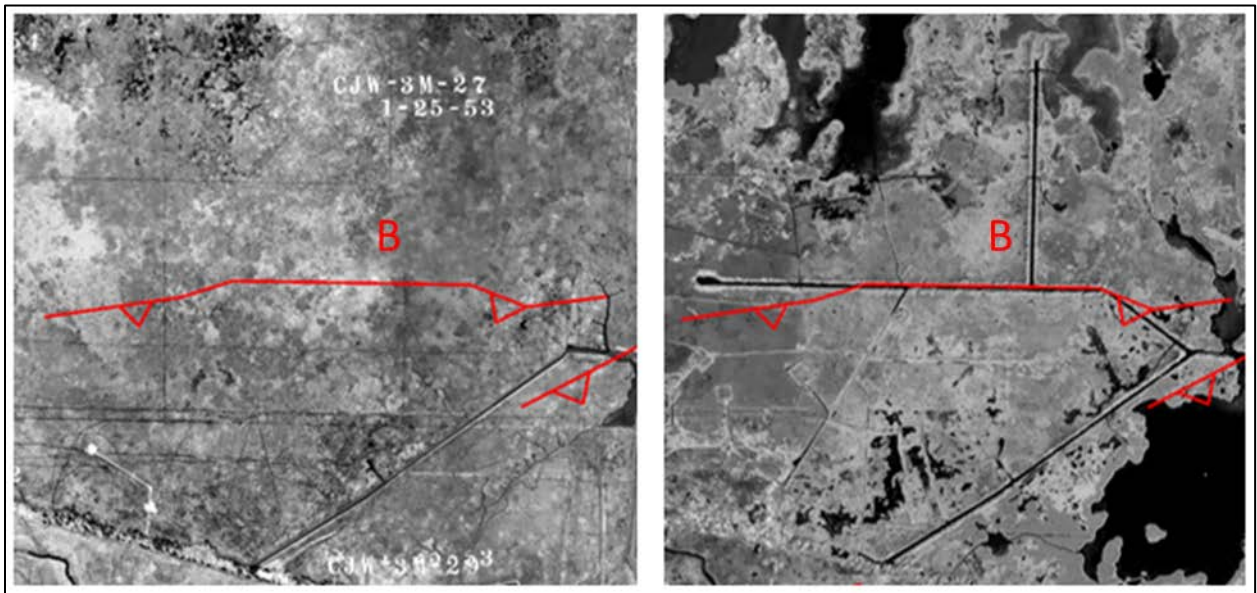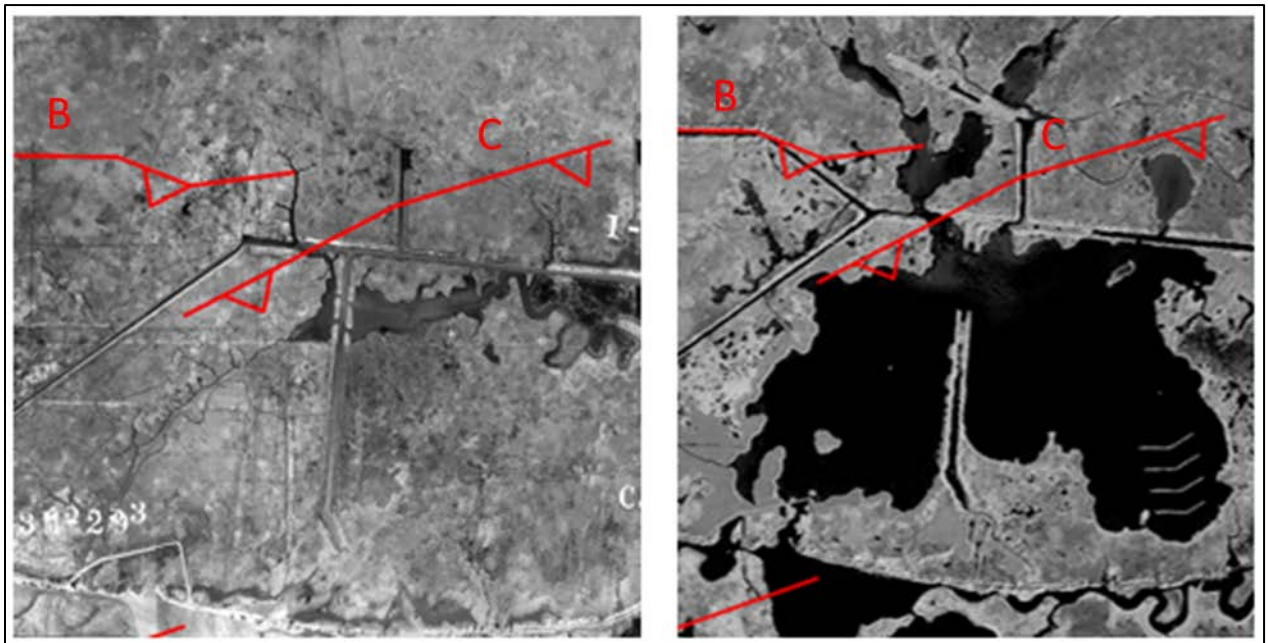

Figure 42: Aerial photograph highlighting Fault A in 1953 (left) and 2017 (right).

4.5.4. Fault D. Fault D occupies one frame, 3M-52, in the 1953 aerial photographs (Figure 43). Land covers both sides of the fault. Minor marsh scarring is present in the west, upthrown to the fault. Chenier Perdue is approximately 2000 ft to the south (0.35 miles). There is a large, 60 acre property on the upthrown side of the fault, where two homes and a maintained lawn occupies the rectangular lot of land. The eastern portion of the fault has a considerable amount of variation in vegetation on the downthrown side of the fault. The modern day images show a medium sized pond occupies the eastern downthrown side of the fault, where the vegetation appeared different. The property on the upthrown side appears to be abandoned. A canal runs along the strike of the suspected fault in the western portion of the fault, this canal was present in 1953 as well.
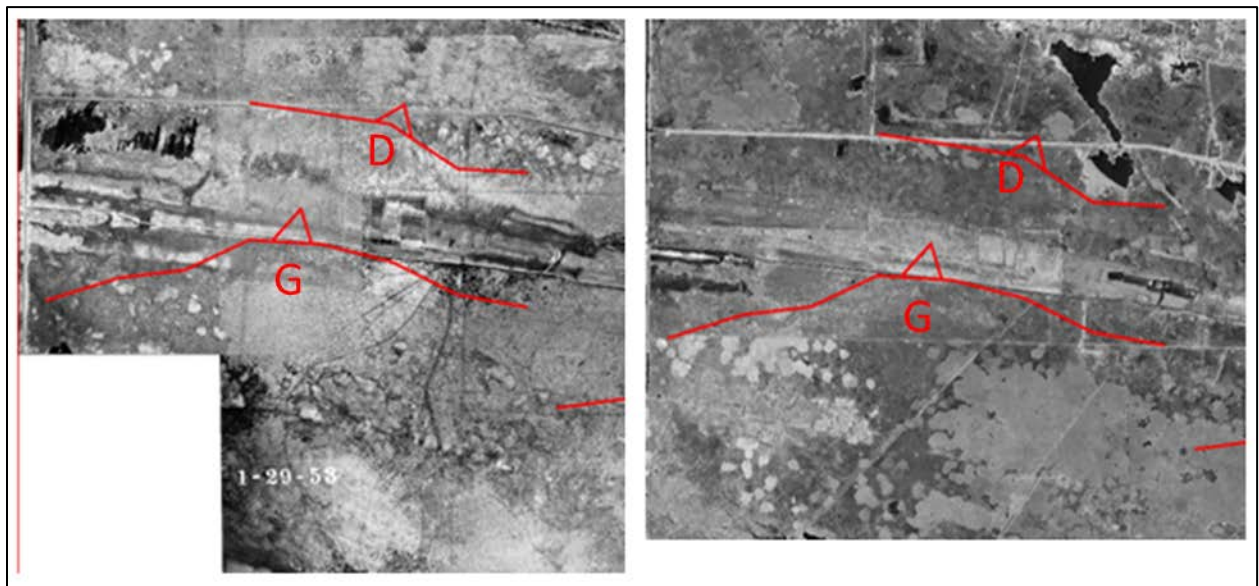
Figure 43: Aerial photograph highlighting Fault D (top), and Fault G (bottom) in 1953 (left) and 2017 (right).

4.5.5. Fault E. Fault E runs through the 1953 frame 3M-27 (Figure 44). The land is heavily scarred on the downthrown side of the fault. In the east, a river runs along the strike of the fault, deviating to the north when it reached the center portion of the fault. A chenier bound its northeast side. The modern day images show open ponds on both the upthrown and downthrown sides of the fault. There are short 400 ft long × 40 ft wide pools offset from each other on the downthrown side (Just interesting).
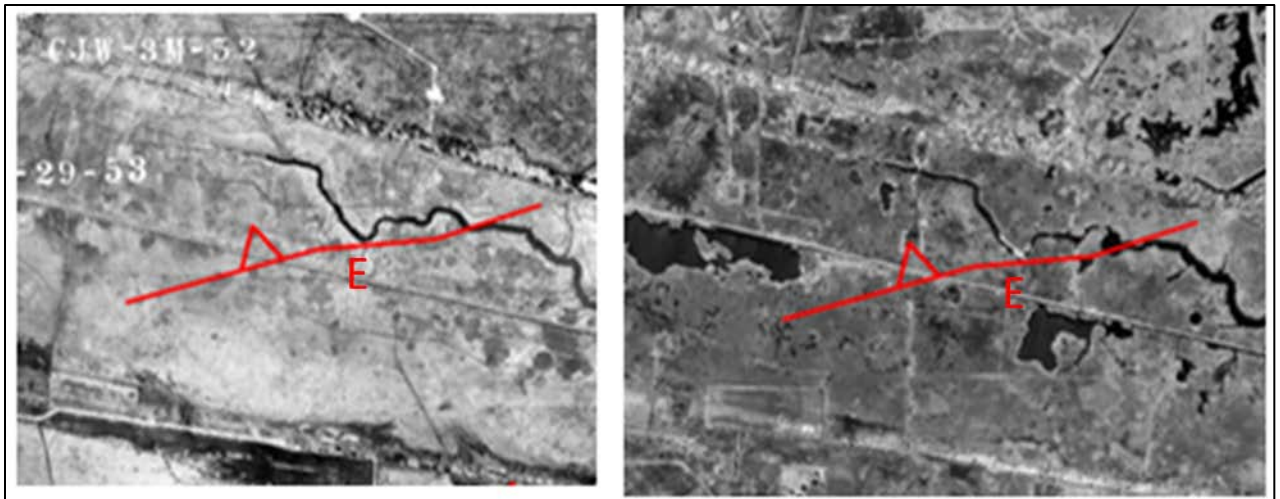
Figure 44: Aerial photograph highlighting Fault E in 1953 (left) and 2017 (right).

4.5.6. Fault F. Fault F is found in two frames from the 1953 aerial photographs (3M-27 and 2M-165) (Figure 45). A large pond can be found 1000 ft to the north. There is a pond on both the upthrown and downthrown sides in the east. Overall, there is good land coverage. The modern day image shows an open pond on the southwest upthrown side of the fault.
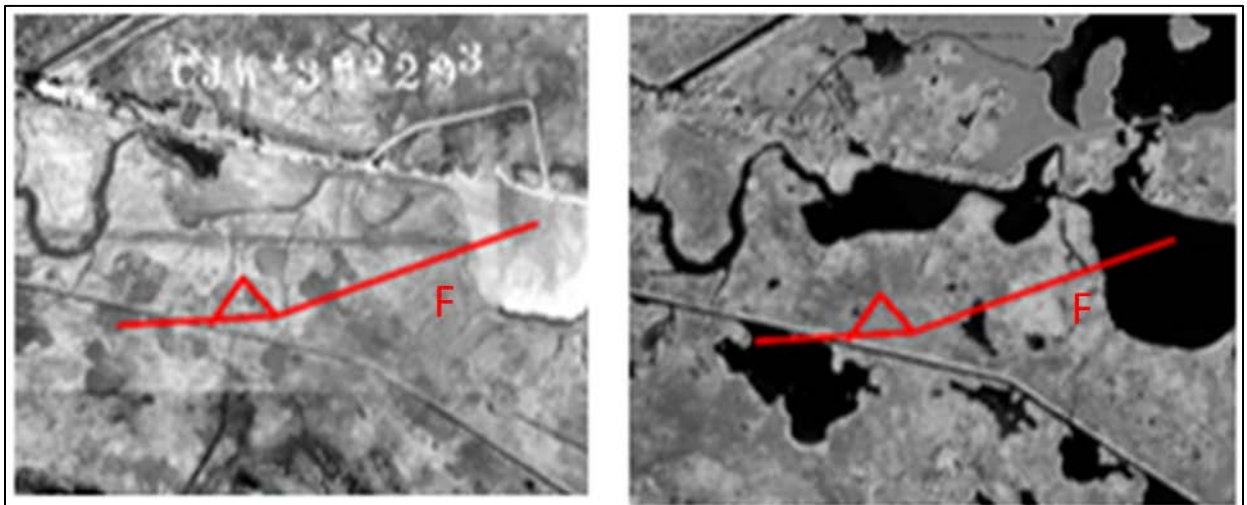
Figure 45: Aerial photograph highlighting Fault F in 1953 (left) and 2017 (right).

4.5.7. Fault G. Fault G is found in two frames from the 1953 aerial photographs (3M-116 and 3M-52) (Figure 37-39 & 43). The downthrown side of the fault runs along the south side of a chenier. Land is present on both sides of the fault. Large variations in terrains along the chenier can be observed, from varied vegetation, marsh burning, and residential property. There is no noticeable difference between the upthrown and downthrown side of the fault however.

4.5.8. Fault H. Fault H is found in one frame from the 1953 aerial photographs (3M-52) (Figure 37-39). Land covers both sides, there is no noticeable surficial evidence of faulting. Minor land scarring is observed. Approximately 3000 ft south of the fault, a 4.5 mile long linear disturbance in the marsh is noticeable running northwest-southeast. The modern day images show no major change in and coverage. There is a stark change in vegetation indicated by infrared is 375 ft north on the downthrown side (well within the error of fault pick).

4.5.9. Fault I. Fault I is found in one frame from the 1953 aerial photographs (3M-29) (Figure 37-39). In the west, the fault runs along the cheniers' south side and crosses over to the north side of the chenier in the east. Marsh was burnt 800 ft to the south. The modern day shows no big change in land coverage. There is possible marsh burning on the upthrown side. A canal is still present running north to south on the western end of the fault.

4.5.10. Fault J. Fault J is found in one frame from the 1953 aerial photographs (2M-163) (Figure 37-39). Approximately 1300 ft to the north a chenier runs along east west. Marsh was burnt in the west. Minor scarring of the landscape appears on either side. The modern day images show more ragged vegetation. Ponding is present on the downthrown side of the fault, on the shore side of the chenier. To the south on the upthrown side, a stream offshoots from the Mermentau River running east west.

5. Discussion

Land loss along the coast of Louisiana is controlled by three main factors: (1) reduced sediment flow from the Mississippi River and its tributaries, (2) sea-level rise, and (3) subsidence. Reduced sediment flow from the Mississippi River and its tributaries is largely responsible for wetland loss in southeastern Louisiana (e.g. Twilley et al., 2016; Chamberlain et al., 2018). However, the Chenier Plains are very different from the Mississippi Delta. The Chenier Plains are a low profile, storm-dominated, micro-tidal coast, down drift, and west of the Mississippi River deltaic plain. They are a sediment starved area, not dependent on sediment supply like the Mississippi Delta, where reduced sediment flow due to river management has been the main factor leading to land loss (Twilley et al., 2016). Instead, sediment build up along the chenier Plains is dependent on longshore drift.

On a longer timescale, sea-level rise poses the greatest threat to Louisiana's coastline (Jankowski et al., 2017; Chamberlain et al., 2018). Recent studies suggest that 35 % of the wetlands in the Mississippi Delta and 58 % in the Chenier Plain may not be able to keep pace with relative sea-level rise (Chamberlain et al., 2018). The rate of relative sea-level rise in southern Louisiana is currently between 4 and 20 mm/year, one of the world's highest (Chamberlain et al., 2018).

Relative sea level rise, however, depends on both eustatic sea-level rise and subsidence. The role of subsidence, and its relationship with active growth faulting, has largely been understudied. Louisiana's coastline is riddled with active growth fault, many of which extend to the surface (e.g. Bruce, 1973). Growth faulting inherently controls subsidence, and must therefore have an impact on land loss.

The data presented here allows us to explore the role of growth faulting on subsidence and associated land loss within a ~ 40 square miles study area located in the Chenier Plains of southern Louisiana. Analysis of the 3D seismic survey reveals the presence of ten faults. These normal faults strike approximately east-west. Three dip to the south, seven to the north, defining an east-west graben that runs nearly in the middle of the study area. The faults were identified in the seismic survey and mapped to the last point of confidence (depth of ~2,000 ft), and extrapolated to the surface by maintaining constant dip. Faults were correlated using well logs for depth <2,000ft, and water well logs and loggers' notes for depth <300ft. Expansion index calculated between undated seismic reflector indicate that, on average, the throw of all the faults increases with depth. Of the 10 faults, 9 exhibit growth in the shallow section. Faults A and C had more than 10% growth and Fault H had as much as 31%.

Fault C is particularly interesting as it was the only fault having a well log on the up- and downthrown side. Fault C also has the largest body of water that is not directly downthrown to it but also conforms to the surface expression of the fault trace. The upper 1,000 feet of sediments are saturated with freshwater. This affects the spontaneous potential and resistivity and is evident in the well log (Figure 19). In this section, sands show a pattern typically seen in shales. Spontaneous potential measures the potential of the formation to transmit electric current. If there are no ions to conduct electricity, the spontaneous potential shows the inverse of typical lithology patterns; sands appear as shales and vice versa, all while the resistivity of the formation is high. In this case, gamma ray logs help identify and confirm that shales are sands and vice versa in this zone. Within the study area, the shallow subsurface (~<100ft) is generally dominated by shale, until reaching the "200 ft sand", which

has been interpreted as the top of the Chicot aquifer and makes for a good correlation maker throughout the field both between electric and driller logs. Correlations across Fault C show that the Chicot Formation top is down dip in the downthrown block to the formation top picked in the upthrown well. This observation is true throughout the study area: many Chicot Formation top picks are down dip, in the graben, from their correlative upthrown picks. Additionally, there is a small, but discernible thickening across this section between the top of the Chicot and the top of the shallow shale. While the well logs do not explicitly indicate offset created by fault, they do point towards a general trend that dips into the graben. Therefore, combined seismic and well data indicate that faults extend almost to the surface, and subsidence appears to be controlled by faulting active today.

To investigate is the subsidence observed in the subsurface had any repercussion at the surface; we used LIDAR data over the study area. Forty-four transect lines made over the LIDAR's digital elevation models reveal that there can be up to 1.5 ft of elevation difference between the up- and downthrown side of some faults. For example, five transect were ran across Fault C, revealing that the mean upthrown elevation is ~1.39 ft and its downthrown is ~0 ft on (Figure 14). Because elevation change is variable along the strike of the faults, we calculated the mean elevation of an area on the up- and downthrown side of the fault. But even by averaging the elevation over an area, we still observed significant elevation changes across the faults; Fault C for example has a mean average of 1.20 ft and 0.91 ft for the up- and downthrown sides, respectively.

The surface difference observed in the vicinity of the fault traces is perhaps even more dramatic when superposing the fault traces on aerial photographs from 1953 to 2017 (Figure 29). In the 1953 aerial photo, a single stream runs sub-parallel along the otherwise solid

ground of Fault C's surface trace (Figure 26). Modern day images show this area is now occupied by a large (1.3 square miles) arcuate pond (Figure 27). Generally, across the study area, the appearance of new or enlarged water bodies between 1953 and 2017 is obvious. Faults A, D, E, F, H and J are all now associated with water bodies that were either nonexistent or much smaller in 1953. Faults E and F withstanding, all of these faults had positive offset indications between their upthrown and downthrown elevation areas. Interestingly, drainage patterns also appear to be influenced across the up- and downthrown sides of the deep-rooted faults. Several streams flow in the middle of the graben formed by the faults.

The relationship between subsidence, compaction, sedimentation, sea level, salinity, vegetation, erosion, and land loss remains complex. However, in the Chenier Plains, a sediment starved area, where sediment loading and compaction are likely insignificant, our results indicate that growth faulting must play an important role in controlling subsidence and associated land loss.

6.   Conclusion

The results from this thesis shed light on the understudied interaction between growth faulting, subsidence, and associated land loss in southwest coastal Louisiana. To understand the important relationship of growth faulting and subsidence, we combined 3D seismic data, well logs, water well logs and loggers notes, LIDAR data, and historical aerial photographs in a study are located in the Chenier Plains of southwestern Louisiana. Results indicate that deep rooted growth faults, and their compensating antithetic faults, reach the surface. Fault offset is confirmed by the LIDAR data. Comparison of aerial photographs from 1953 and 2017 indicates that the downthrown side of the faults is occupied by water bodies and has experienced land loss. The causal effect of faults reaching the surface is lowering ground-level on the downthrown side of the faults contributing to subsidence, and, ultimately land loss when lowered below sea level. Faults may also play a role in controlling the geomorphology, hydrologic drainage, and vegetation growth.

References

Antonie, J. and W. R. Bryant, 1969, Distribution of salt and salt structure in the Gulf of Mexico: AAPG Bulletin, v. 53, p. 2543-2550.

Bearb, N.A., 2013. Sedimentology of the Miocene Bigenerina humblei and Amphistegina "B" Sandstones inHog Bayou Field, Offshore Block East Cameron 1 and Cameron Parish, Louisiana: A Well Log Based Study: *UL Master's Theses.*

Bird, D. E., K. Burke, S. A. Hall, and J. F. Casey, 2005, Gulf of Mexico tectonic history: Hotspot tracks, crustal boundaries, and early salt distribution: AAPG Bulletin , v. 89, no. 3, p. 311-328.

Bornhauser, M., 1958, Gulf Coast tectonics: American Association of Petroleum Geologists Bulletin, v. 42, p. 339-370.

Bruce, C. H., 1973, Pressured shale and related sediment deformation: mechanisms for development of regional contemporaneous faults: American Association of Petroleum Geologists Bulletin, v. 57, p. 878-886.

Cahoon, D.R., Reed, D.J., Day, J.W., Jr., Steyer, G.D., Boumans, R.M., Lynch, J.C., Mcnally, D., And Latif, N., 1995, The influence of Hurricane Andrew on sediment distribution in Louisiana coastal marshes: Journal of Coastal Research, Special Issue, v. 18, p. 280-294.

Chamberlain, E. L., Törnqvist, T. E., Shen, Z., Mauz, B., & Wallinga, J. (2018). Anatomy of Mississippi Delta growth and its implications for coastal restoration. Science advances, 4(4), eaar4740.

Dokka, R. K., 2006, Modern-day tectonic subsidence in coastal Louisiana, Geology, v. 34, p. 281–284. Dokka, R. K., 2011, The role of deep processes in late 20th century subsidence of New Orleans and coastal areas of southern Louisiana and Mississippi, J. Geophys. Res.,

Dokka, R. K., 2011, The role of deep processes in late 20th century subsidence of New Orleans and coastal areas of southern Louisiana and Mississippi, J. Geophys. Res.,

Fails, T. G., 1990, Variations in salt dome faulting, coastal salt basin: Gulf Coast Association of Geological Societies Transactions, v. 5, p. 89-86

Fisk, H. N., and E. McFarlan, Jr., 1955, Late Quaternary deltaic deposits of the Mississippi River: Geol. Soc. America Special Paper 62, p. 297-302

Gagliano, S.M., Kemp, E.B.,Wicker, K.M., Wiltenmuth, K.S., Sabate, R.W., 2003, Neo-tectonic Framework of Southeast Louisiana and Applications to Coastal Restoration: Gulf Coast Association of Geological Societies, v. 53, pp. 262-272

Galloway, W. E., N. Buster, 2011, A.Gulf of Mexico Origin, Waters and Biota Volume 3: Geology; Pre-Holocene Geological Evolution of the Northern Gulf of Mexico Basin (1 ed.). Corpus Christi: Texan A&M University Press. p 33-48.

González, J. L., and T. E. Törnqvist, 2006, Coastal Louisiana in crisis: Subsidence or sea level rise?: EOS, Transactions of the American Geophysical Union, v. 87, p. 493 and 498.

Gosselink, J. G., C. L. Cordes, and J. W. Parsons, 1979, An Ecological Characterization Study of the Chenier Plain Coastal Ecosystem of Louisiana and Texas: U.S. Fish and Wildlife Service, Office of Biological Sciences. FWS/OBS-78/9 through 78/11.

Gould, H. R., and E. McFarlan, Jr., 1959, Geologic History of the Chenier Plain, Southwestern Louisiana: Transactions-Gulf Coast Association of Geological Societies, v. 9, p. 261-270.

Heinrich, P.V., 2000. DeQuincy Fault-Line Scarp, Beauregard and Calcasieu Parishes,

Louisiana: Basin Research Institute Bulletin, v. 9, pp. 38-50.

Heltz, J. O., 2005, Evidence of neotectonic activity in southwest Louisiana: *LSU Master's Theses*. 3177

Howe, H.V., R.J. Russell, and J.H. McGuirt., 1935, Physiography of coastal southwest Louisiana: Louisiana Geological Survey Bulletin, v. 6, p. 1–68.

Howe, H. V., R. J. Russell, J. H. McGuirt, B. C. Craft, and M. B. Stephenson, 1935, Reports on the Geology of Cameron and Vermilion Parishes: New Orleans Department of Conservation, Louisiana Geological Survey, Geological Bulletin 6.

Hoyt, J. H., 1969, Chenier Versus Barrier, Genetic and Stratigraphic Distinction, American Association of Petroleum Geologists Bulletin. v. 53, No. 2, p. 299-305.

Jankowski, K. L., Törnqvist, T. E., & Fernandes, A. M. (2017). Vulnerability of Louisiana's coastal wetlands to present-day rates of relative sea-level rise. Nature Communications, 8, 14792.

Kuecher, G. J., 1994 Geologic Framework and Consolidation Settlement Potential of the Lafourche Delta, Topstratum Valley Fill; Implications for Wetland Loss in Terrebonne and Lafourche Parishes, Louisiana. LSU Historical Dissertations and Theses. 5734.

Kuecher, G. J., 1995, The dominant processes responsible for subsidence of coastal wetlands in south Louisiana, in Land Subsidence: Proceedings of the Fifth International Symposium on Land Subsidence, edited by F. J. Barends et al., pp. 69-81, Int. Assoc. of Hydrol. Sci., The Hague, Netherlands.

Martin, R. G., 1978, Northern and eastern Gulf of Mexico continental margin: stratigraphic and structural framework: AAPG Studies in Geology No. 7, p. 21-42.

May, P. R., 1971, Pattern of Triassic-Jurassic dikes around the North Atlantic in the context of pre-drift positions of the continents: GSA Bulletin, v. 82, p. 1285-1292.

McBride, R. A., M. J. Taylor, and M. R. Byrnes, 2007, Coastal morphodynamics and Chenier Plain evolution in southwestern Louisiana, USA: A geomorphic model: Geomorphology, v. 88, p. 367-422.

McLean, C. M., 1957, Miocene geology of southeastern Louisiana: Transactions, Gulf Coast Association Geological Societies, v. 7, p. 241-45.

Nevitt, S., 2017. Organic Geochemical Proxies as Indicators of Paleoenvironmental Conditions and Source Sediment Provenance in the Chenier Plain, Vermilion and Cameron Parishes,

Louisiana, USA: *UL Master's Theses.*

Nienhuis, J. H., Tornqvist, T. E., Jankowski, K. L., Fernandes, A. M., and Keogh, M. E., 2017. A new subsidence map for coastal Louisiana. GSA Today, 27, 58-59.

Nyman, J. A., C. R. Crozier, and R. D. Delaune, 1995, Roles and patterns of hurricane sedimentation in an estuarine marsh landscape: Estuarine, Coastal and Shelf Science, v. 40, p. 665-679.

Ocamb, R. D., 1961, Growth faults of south Louisiana: Gulf Coast Association of Geological Societies Transactions, v.11, p. 139-175.

Owen, D.E., 2008, Geology of the Chenier Plain of Cameron Parish, southwestern Louisiana, in Moore, G., ed.: Geological Society of America Field Guide 14, 2008 Joint Annual Meeting, Houston, Texas, 5–9 October 2008, p. 27–38.

Owen, D.E., 2008, Geology of the Chenier Plain of Cameron Parish, southwestern Louisiana: Geological Society of America Field Guide 14, 2008 Joint Annual Meeting, Houston, Texas, 5–9 October 2008, p. 27–38, doi: 10.1130/2008.fld014(02).

Penland, S., and J. R. Suter, 1989, The Geomorphology of the Mississippi River chenier plain: Marine Geology, v. 90, p. 231-258.

Russell, R.J., and H.V. Howe., 1935, Cheniers of southwestern Louisiana: Geographical

Review, v. 25, p. 449–461, doi: 10.2307/209313.

Salvador, A., 1987, Late Triassic-Jurassic Paleogeography and Origin of Gulf of Mexico Basin: The American Association of Petroleum Geologists Bulletin, v. 71, no. 4, p. 419-451.

Scholz, C.H., 1998. Earthquakes and friction laws: Nature, v. 391. no. 6662, pp. 37-42.

Tearpock, D. J., and R. E. Bischke, 1991, Applied subsurface geological mapping, p. 256 - 264.

Thorsen, C. E., 1963, Age of Growth Faulting in Southeast Louisiana: Transactions – Gulf Coast Association of Geological Societies, v 13, p. 103-110.

Törnqvist, T. E., J. L. González, L. A. Newsom, K. van der Borg, A. F. M. de Jong, and C. W. Kurnik, 2004, Deciphering Holocene sea-level history on the U.S. Gulf Coast; a high- resolution record from the Mississippi Delta: Geological Society of America Bulletin, v. 116, p. 1026-1039, doi: 10.1130/B2525478.1.

Tornqvist, T. E., S. J. Blick, K. van der Borg, and A. F. M. deJong, 2006, How stable is the Mississippi Delta?: Geology, v. 34, p. 697-700.

Turner, R. E., J. J. Baustian, E. M. Swenson., and J. M. Spicer, 2006, Wetland Sedimentation from Hurricanes Katrina and Rita: Science, v. 314, p. 449-452.

Tweel, A. W., and R. E. Turner, 2012, Landscape-Scale Analysis of Wetland Sediment Deposition from Four Tropical Cyclone Events: PLoS One, v. 7-11, p. 1-10.

Tweel, A. W., and R. E. Turner, 2014, Contribution of Tropical Cyclones to the Sediment Budget for Coastal Wetlands in Louisiana, USA: Landscape Ecology, v. 29, p.1083-1094. doi10.1007/s10980-014-0047-6.

Twilley, Robert R. et al. "Co-evolution of wetland landscapes, flooding, and human settlement in the Mississippi River Delta Plain." 26 May 2016.

Worrall, D.M., and S. Snelson, 1989. Evolution of the northern Gulf of Mexico, in Bally, A.W.,

and Palmer A.R., eds., The Geology of North America—An overview, Boulder, Colorado,

Geological Society of America, Geology of North America, v. A, pp. 97-138.

Verbeek, E. R., U. S., Clanton, 1981, Historically Active Faults In The Houston Metropolitan Area, Texas: U.S. Geological Survey,

Yang, S. Y, 1991, Structure and stratigraphy of West and East Cameron and neighboring OCS areas, offshore western Louisiana, Gulf of Mexico: Ph.D. dissertation, Texas A&M University, 111 p.
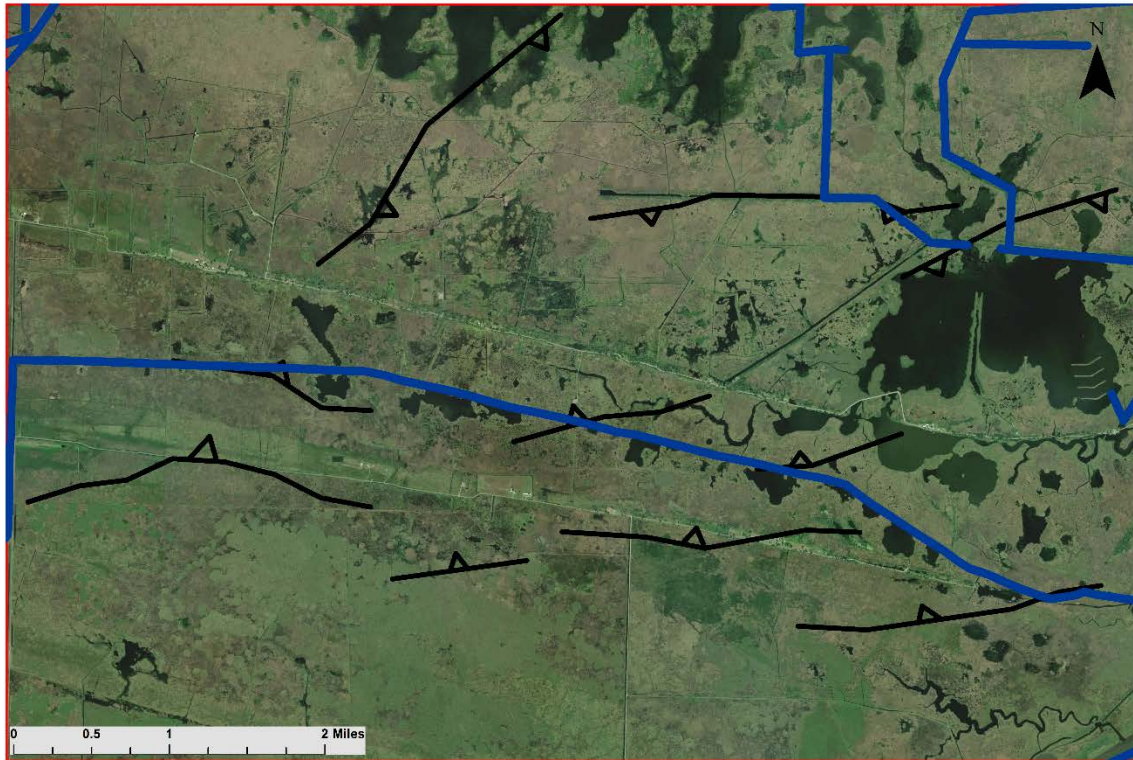
Appendix A

Graben
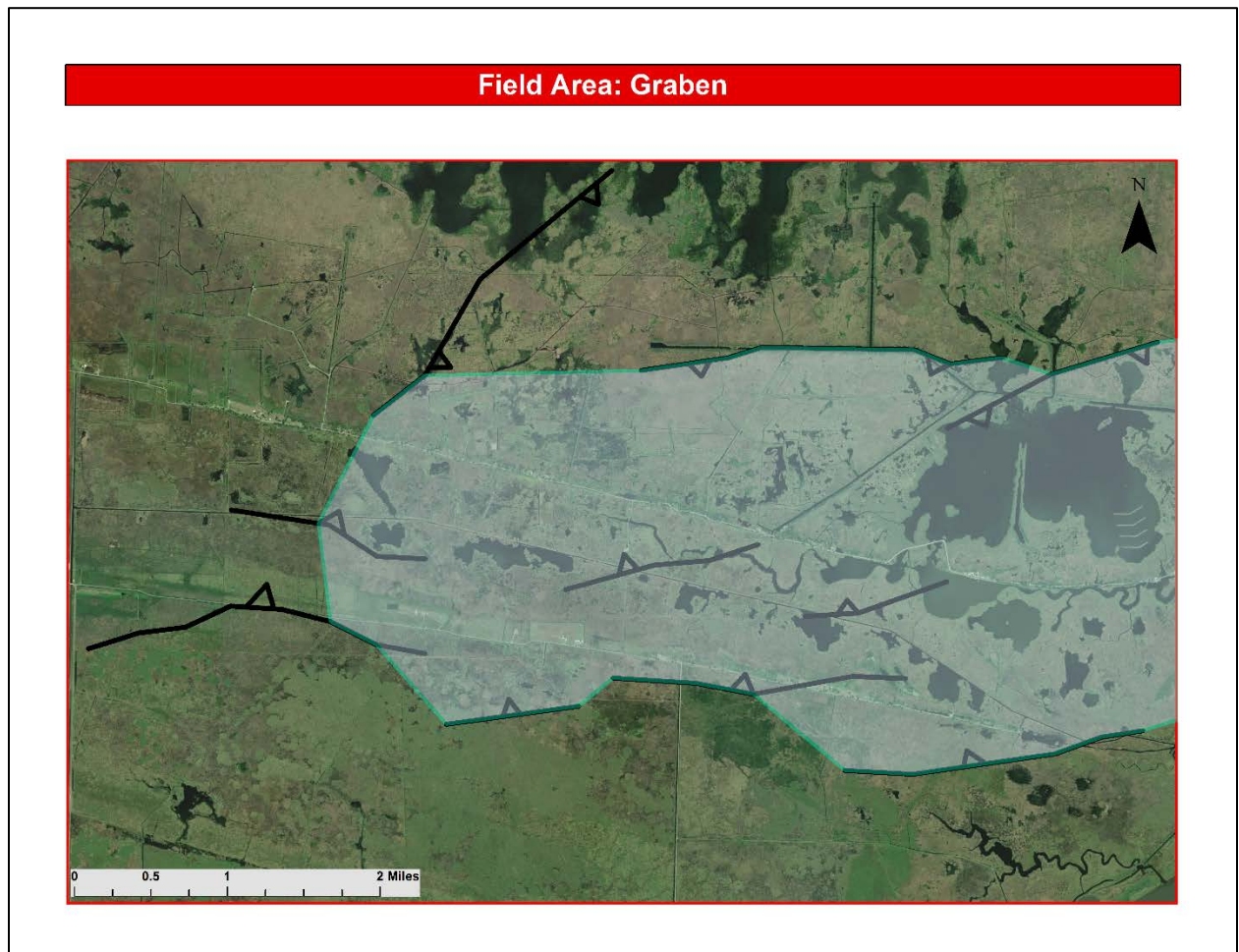
Field Area: Graben

Black lines represent fault surfaces. The light blue polygon represents the graben feature of this field

Field Area: Hydrologic Model

Black lines represent fault surfaces. Blue lines represent the channel flow modeling component of the Chenier Plain Regional Model implemented in the Southwest Coastal Louisiana Feasibility Study. Sourced from the Institute of Coastal Ecology and Engineering, Department of Civil Engineering, University of Louisiana at Lafayette

Appendix B
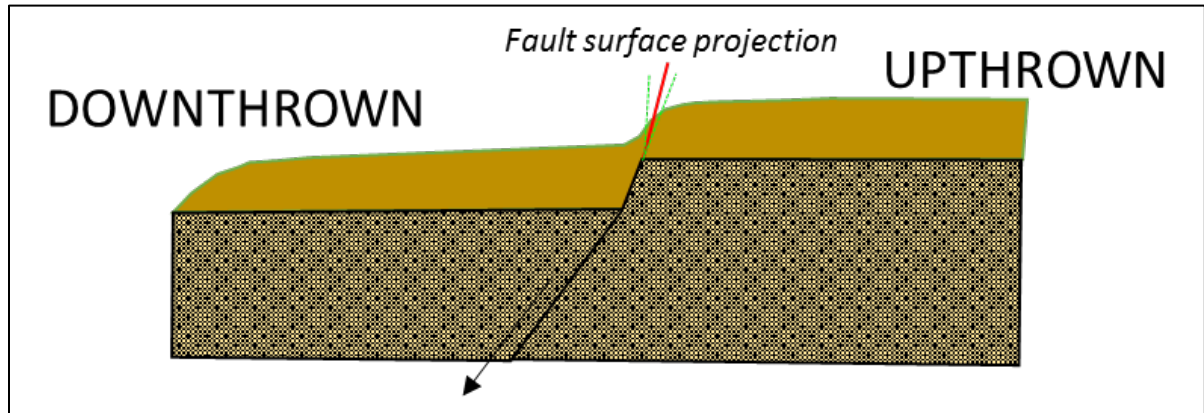
Cartoon of surficial expression fault. Extrapolation (red) and error (green).

Biographical Sketch

Matthew Covington O'Leary was born in New Orleans on September 17th, 1992. He grew up in New Orleans, Louisiana, where he attended St. Andrews Episcopal School and then graduated from Isidore Newman. Following his high school graduation, he enrolled in the geology program at Louisiana State University. At LSU, he received his Bachelor of Science in Geology in May, 2015. After receiving his Bachelor of Science degree, he enrolled in the graduate school at the University of Louisiana at Lafayette. He will complete the requirements for a Master of Science in Geology in the summer of 2018.